CONT.

AD A103571

BASIC EROSION INVESTIGATION IN SMALL TURBOMACHINERY

FINAL REPORT

BY

W. TABAKOFF AND T. WAKEMAN

JULY 1981

DTIC FILE COPY

81 9 01 092

SECURITY CLASSIFICATION OF THIS PAGE (When Data Entered)

REPORT DOCUMENTATION PAGE	READ INSTRUCTIONS BEFORE COMPLETING FORM

1. REPORT NUMBER	2. GOVT ACCESSION NO. AD-AJ03571	3. RECIPIENT'S CATALOG NUMBER

4. TITLE (and Subtitle) Basic Erosion Investigation in Small Turbomachinery	5. TYPE OF REPORT & PERIOD COVERED
	6. PERFORMING ORG. REPORT NUMBER 81-52

7. AUTHOR(s) W. Tabakoff and T. Wakeman	8. CONTRACT OR GRANT NUMBER(s) DAAG-29-76-0229

9. PERFORMING ORGANIZATION NAME AND ADDRESS University of Cincinnati Cincinnati, Ohio 45221	10. PROGRAM ELEMENT, PROJECT, TASK AREA & WORK UNIT NUMBERS

11. CONTROLLING OFFICE NAME AND ADDRESS U.S. Research Office, Research Triangle Park, NC 27709	12. REPORT DATE July 1981
	13. NUMBER OF PAGES 74

14. MONITORING AGENCY NAME & ADDRESS(If different from Controlling Office)	15. SECURITY CLASS. (of this report) Unclassified
	15a. DECLASSIFICATION/DOWNGRADING SCHEDULE

16. DISTRIBUTION STATEMENT (of this Report)

Distribution Unlimited

17. DISTRIBUTION STATEMENT (of the abstract entered in Block 20, If different from Report)

18. SUPPLEMENTARY NOTES

19. KEY WORDS (Continue on reverse side if necessary and identify by block number)

Erosion

20. ABSTRACT (Continue on reverse side if necessary and identify by block number)

Description of the high temperature erosion facility at the University of Cincinnati is presented. A large portion of this investigation is devoted to the measurement and prediction of particle rebound characteristics. The abrasive particles were silica sand with average diameters of 165 microns impacting on the following materials: INCO 718, Ti 6-4, 2024 AL, RENE 150, Lead and Berillium. In addition, measurements of erosion rates were

DD FORM 1473 EDITION OF 1 NOV 65 IS OBSOLETE

SECURITY CLASSIFICATION OF THIS PAGE (When Data Entered)

were performed for materials used in jet engine blades. Semi-empirical equations were developed to predict erosion rates for INCO 718, Ti 6-4 and 2024 AL target materials.

ACKNOWLEDGEMENT

TABLE OF CONTENTS

LIST OF FIGURES

LIST OF TABLES

ABSTRACT

Description of the high temperature erosion facility at the University of Cincinnati is presented. A large portion of this investigation is devoted to the measurement and prediction of particle rebound characteristics. The abrasive particles were silica sand with average diameters of 165 microns impacting on the following materials: INCO 718, Ti 6-4, 2024 AL, RENE 150, Lead and Berillium. In addition, measurements of erosion rates were performed for materials used in jet engine blades. Semi-empirical equations were developed to predict erosion rates for INCO 718, Ti 6-4 and 2024 AL target materials.

NOMENCLATURE

e	restitution ratio
I	impulse
L	length of particle streak on screen, m.
n	length traveled by particles between two successive frames, m.
R	reference line projected on screen, m.
r	actual length of reference line, m.
S	film speed (local), m/s.
t_c	exposure time of frame observed, s.
V	particle velocity, m/s.
W	work.
Y_S	yield strength.
β	angle of attack.
ε	erosion rate.

Subscripts

1	incoming.
2	rebounding.
G	mass.
N	normal.
T	tangential.
V	vertical, or volume.
β	angle.

INTRODUCTION

In many industrial and military applications, including
jet engines, erosive action of high-speed particles results
in performance deterioration. Erosion has been pointed out
as a problem in diverse areas such as gas turbines, rocket
nozzles, coal fired boilers and many others. Filtration of
the erosive particulate is one method of reducing the erosive
damage, however, filtration usually reduces the system per-
formance and for many aircraft applications, it is impractical.
Accurate prediction of erosion patterns and rates in an erosion
sensitive machine on the other hand, may indicate designs which
minimize the erosive damage and the performance determination
effect. The aim of this investigation is to improve the state
of the art in predicting erosion pattern and rates. Two
problems are involved in erosion prediction. First, the velocity,
direction and number of particles striking the surface must be
determined. These are naturally affected by the general and
local flow conditions. The second part involves the calculation
of the surface material removed using the information obtained
from the first part. The problem of predicting erosion in
rotating machinery is particularly complicated by multiple
impacts and rebounds [1].

A large portion of this investigation is devoted to the
measurement and prediction of particle rebound characteristics.
The particle rebound characteristics were measured for 165μ
silica sand particles impacting on the following target materials:
INCO 718, Ti 6-4, 2024 AL, RENE 150 Lead and Berillium. In
addition, empirical equations were generated from this data
to predict particle rebound characteristics for INCO 718,
Ti 6-4 and 2024 AL target materials. Particle rebound characteristics
were measured relative to particle impingement angle and velocity
at elevated target temperatures. The present study represents
the first in depth investigation of target temperature on

1

rebound characteristics. The target temperatures were varied
between ambient and 1600°F consistent with the technical
capabilities of the tested materials.

The materials selection for testing was based on their
use as compressor and turbine blade materials in jet engines.
Lead and Berillium were tested because of their difference
relative to the other materials tested. Silica sand 165µ
was selected as the erosive particulate because it is repre-
sentative of particulate entering a jet engine operating in
dusty terrain.

Another significant portion of the present investigation
consists of the measurement and prediction of erosion rates.
Erosion rates were measured for the target materials listed
above impacted by 165µ silica sand. Semi-empirical equations
were developed to predict erosion rates for INCO 718, Ti 6-4
and 2024 AL target materials. This investigation presents
the first significant materials erosion rate data obtained
at the jet engine operating temperatures.

The erosion rate prediction equations combine the infor-
mation provided from the erosion rate measurements with that
obtained from the rebound characteristics. For measurements
of the erosion rates and the particle rebound characteristics,
a high temperature erosion facility was designed and installed
at the University of Cincinnati Propulsion and Fluids Laboratory.

2

PRESENT STATE OF THE ART

The problem of predicting erosion in rotating machinery is particularly complicated by multiple impacts. The theoretical studies concerning erosion are predominantly empirical. They involve basic assumptions as to the process governing material removal. Finnie [2] and Smeltzer et al. [3] have conducted theoretical analyses of the erosion of ductile materials. In more recent investigations [1,4,5], further insight into the actual mechanism of erosion has been obtained by examining the target surface at high magnification using metallographic techniques and electron microscopy. A detailed description of these test facilities at the University of Cincinnati's Propulsion and Fluids Laboratory can be found in references [1] and [6].

In many turbomachinery applications, erosion takes place at elevated temperatures near the strength limiting temperatures of the materials used. For example, even in the case of turbojet engine compressors, titanium used in the early stages and the INCO 718 used in the aft stages are operated at metal temperatures in excess of 316 and 593°C (600 and 1100°F), respectively. In both cases, these temperatures are very close to the maximum operating temperatures used for these materials. The erosion characteristics can significantly change under elevated temperatures, as evidenced in the data presented by Tabakoff and Hamed [6]. These data were obtained with the sample heated to temperatures up to 204°C (400°F). Although this temperature falls far short of those experienced in turbine engines, it still indicates the significant effect of temperature on erosion and probably on the rebound characteristics.

3

HIGH-TEMPERATURE EROSION FACILITY

An erosion test facility was designed to provide erosion and rebound data in the range of operating temperatures experienced in compressors and turbines. For that purpose, this facility has been designated to operate at a test section temperature in the range of ambient to 1093°C (2000°F). In addition to high temperatures, the facility properly simulates all erosion parameters which were found to be important from previous testing at ambient temperatures. These parameters include particle velocity, angle of impact, particle size, particle concentration, and sample size. Close attention was given to aerodynamic effects to insure that important parameters, such as angle of attack, are not masked or altered.

General Description of High-Temperature Erosion Rig

A schematic of the test apparatus is shown in Fig. 1; it consists of the following components: particle feeder (A), main air supply pipe (B), combustor (C), particle preheater (D), particle injector (E), acceleration tunnel (F), test section (G), and exhaust tank (H).

The equipment functions as follows. A measured amount of abrasive grit of a given constituency is placed into the particle feeder (A). The particles are fed into a secondary air source and blown up to the particle preheater (D), and then to the injector (E), where they mix with the main air supply (B), which is heated by the combustor (C). The particles are then accelerated by the high-velocity air in a constant-area steam-cooled duct (F) and impact the specimen in the test section (G). The particulate flow is then mixed with the coolant and dumped in the exhaust tank. This facility is capable of supplying erosion data at temperatures in the range of ambient to 1093°C (2000°F). The expected range of testing parameters is given in Table 1, but is not necessarily restricted to the tabulated values.

4

TABLE 1 - EROSION PARAMETERS

Parameters	
Temperature	10 to 1093°C (50 to 2000°F)
Particle angle of attack	0 to 90 deg
Particle velocity	60 to 450 m/s (200 to 1500 ft/s)
Particle concentration	0 to 5 percent
Particle size	1 to 2000 μm
Particle type and material	silica sand, alumina, ash
Specimen size	6.35 to 25.4 mm (1/4 to 1 in.)
Specimen material	various jet engine materials

The individual components which make up the high-temperature erosion facility are described in the following. Each component was designed with cost, maintainability, availability, and functionality as prime considerations.

Particle Feeder Assembly (A) - The particles from the feeder (Fig. 2) are blown up to the particle injector area. The feeder is designed as a pressure vessel to operate at high air pressures. However, this pressure is equalized above and below the plunger by a bypass line. This allows the system to be calibrated under gravity feed conditions. Further, an electric eye records the plunger rpm such that the operating conditions are maintained. The metering orifice is designed to be replaceable. In this manner, a larger (or smaller) orifice may be used, along with corresponding rod diameter, to allow versatility of the feeder.

Main Air Supply (B) - This air is drawn from air tank storages, which allow continuous testing.

Combustor (C) - High-temperature combustion products are supplied by a modified General Electric J93 can combustor as shown in Fig. 3. The J93 can is encased in a 228.6 mm (9 in.) inside-diameter stainless steel pipe with provisions for the fuel nozzle and igniter. Due to heat loss in the acceleration tunnel, achieving the maximum test section temperature of 1093°C (2000°F) requires a combustor exit temperature of 1204.4°C (2200°F).

5

To obtain this temperature from a J93 can combustor, certain modifications were required, including use of a large fuel nozzle and blanking off most of the downstream dilution air ports. In order to obtain low combustion temperatures in the range of 93 through 260°F (200 through 500°F), a smaller fuel nozzle is used. The fuel is ignited by a system consisting primarily of a propane-fired torch containing a spark plug.

Particle Preheater (D) and Injector (E) - The preheater consists of a coil contained in a 203.2 mm (8 in.) inside-diameter pipe section with a distributor/injector to provide a well-distributed preheated particle supply (Fig. 1). The particles are blown up to the accelerating section of the tunnel by secondary air which flows from the particle feeder and passes through the preheater coils. As the particulate air mixture passes through the coils, it is heated by the combustion products to a temperature of 538°C (1000°F) before being injected into the tunnel. The spread-out of the particles in the main airstream is accomplished by impinging them on a specially contoured ball, and then accelerating them through an elliptical nozzle to the acceleration duct section.

Acceleration Section (F) - Figure 4 shows the acceleration section, which is 3.66 m (12 ft) long with a rectangular cross section 89 by 25.4 mm (3 1/2 by 1 in.)]. The acceleration tunnel is steam cooled to minimize heat loss. The use of steam coolant allows the 316 stainless steel liner to operate at a maximum of 760°C (1400°F). This maximum operating temperature results in a temperature drop in the gas stream of about 93°C (200°F) which is quite acceptable. The use of water as a coolant would have resulted in at least three times the heat loss.

The particle velocities attained in this acceleration section are predicted analytically and verified by experimental methods. Since the particles are accelerated by aerodynamic drag forces imparted by the high-velocity air, it is necessary to know the air velocity at all locations in the tunnel. For

6

this reason, the tunnel pressure is measured at the inlet, midsection, and exhaust.

Test Section (G) - The test section (Fig. 1) is designed such that the particle-laden air is channeled over the specimen and the aerodynamics of the fluid surrounding the test specimen are preserved. This section contains several interchangeable inserts such that the fluid profile can be determined using conventional instrumentation, and the particle trajectories can be recorded using high-speed photographic methods.

The test specimen can be oriented at different angles to the gas stream by rotating the specimen holder. The test section flow path turns 30 degrees at the plane of the test section to help turn the flow when the test specimen is oriented at an angle. The test section is water-cooled. This does not significantly cool the primary gas stream due to the section's small size. The coolant water is discharged into the particulate gas stream at the test section.

Testing of particle rebound characteristics is accomplished using photographic means to measure the speed and angle of the impinging and rebounding particles. For this purpose, a special test section with a glass window was constructed.

Exhaust System (H) - The erosion rig exhaust system consists primarily of a settling tank (Fig. 1). The exhaust from the erosion test section is loaded with cooling water. In the settling tank, the water is removed from the air, taking with it most of the erosion particles. The particle-laden water is drained from the bottom of the tank through a 101.6 mm (4 in.) line. The air leaves the top of the tank through a 152.4 mm (6 in.) line which discharges the air outside the building. The steam used in cooling the 3.66 m (12 ft) acceleration tunnel is also discharged through the same exit line. A more detailed description of this test facility may be found in reference [7].

7

Tunnel Instrumentation and Calibration

Details of the High Temperature Erosion facility instru-
mentation and its use is described in Table 2. All fluid flows
pressures and temperatures are measured along with critical
metal temperatures.

TABLE 2 - INSTRUMENTATION

Quantity	Description	Use
1	Fuel flow	Total tunnel flow
1	Burner end total temperatures	Tunnel inlet Mach No.
1	Burner end total pressure	Tunnel inlet Mach No.
1	Tunnel entrance static pressure	Tunnel inlet Mach No.
2	Test section static pressure	Tunnel pressure drop test section Mach No.
2	5-element combination total pressure and temperature rakes	Tunnel calibration tunnel end Mach No.
8	Tunnel metal temperatures	Safety, aero-calculations and sample temperature
4	Sample metal temperatures	Sample temperature calibration
4	Steam flow & temperatures	Heat flux calibration

Burner exit conditions were measured to determine the tunnel
friction factor. In addition, the tunnel exit gas temperature
is measured and compared with the burner exit gas temperature.
The measured fuel flow is used to calculate the total gas flows
and the combustor performance.

An *instrumented target sample* was installed to calibrate
the sample temperature versus the more easily measured burner
exit temperature. It was found that the measured sample temperature

is approximately identical to the measured tunnel exit gas temperature.

General Description of Test Programs

The previously described high temperature material erosion facility was used to obtain basic erosion rate and particle rebound data for the target materials of INCO 718, Ti 6-4, 2024 AL, R 150, Lead and Berillium. In all cases, 165μ average particulate size quartz sand (SiO_2) was used as the abrasive. This particle size varied between 150 and 180μ. Experimental measurements were obtained for sand-particle velocities varying from 45.7 m/s (150 ft/sec) to 320 m/s (1050 ft/sec), and target temperature varying from ambient to 788°C (1450°F). Approximately 20% of the test points were repeated and the facility was calibrated at approximately 100 test-point intervals to assure uniformity of data. Several test points were accumulated with no particle injection resulting in negligible change in target weight. This confirmed that oxidation and corrosion of the target material was insignificant as expected, due to the shortest duration (less than 5 minutes test temperature).

Particle velocity was controlled by varying the tunnel air flow. The particle impingement angle was set by rotating the sample relative to the flow stream direction. Sample temperature was varied by heating the flow stream which heated the material sample to the desired temperature. Aerodynamic effects are preserved by the test section tunnel design. Flow conditions in the tunnel provide the aerodynamics around the blades sample.

Particle Rebound Test

Particle rebound data was generated for 157-177μ silica sand particles impinging on the following target materials: 2024 AL, Ti 6-4, INCO 718, Lead and DSR-150. For the DSR-150 the unidirectional material grains were oriented both parallel

9

and normal to the measurement plane.

Rebound characteristics were generated as a function of the same parameters found to be important in material erosion. These parameters are impingement angle, impingement velocity, and target temperature. A summary of the target materials, temperatures, impingement angles and velocities for the particle rebound test data is given in Table 3.

TABLE 3 - PARTICLE REBOUND TEST SUMMARY

Target Material	No. of Test Points	Target Temp. °C (°F)	Impingement Angle, °	Impingement Velocity m/s (ft/sec)
Ti 6-4	29	Ambient to 699 (1200)	45, 60, 90°	63.4 (208) to 153 (503)
INCO 718	14	Ambient to 649 (1200)	25, 35, 45, 90°	69.2 (227) to 170 (559)
2024 AL	12	Ambient to 482 (800)	25, 45, 90°	65.5 (215) to 164 (539)
DSR 150	4	Ambient	45, 90° 2 Grain Orientation	76.2 (250)
Lead	4	Ambient	25, 45, 90°	76.2 (250)
Berillium	4	Ambient	45, 90°	76.2 (250)

Analysis of Photographic Data

Two techniques of analyses were used in reducing the photographic data. These techniques are complimentary in that one was used to check the other. Both of these methods relied on a reference distance which was marked on the test section background. The particle velocities were obtained by comparing the distance traveled by the particle in two successive frames to this reference distance.

10

The first method of analysis is essentially one of streak photography. The velocity is determined by dividing the distance traveled by the particle during the exposure for one frame.

The velocity is calculated using

$$V = (L \frac{r}{R}) \mid t_c \tag{1}$$

where

V = particle velocity, m/s,

L = length of particle streak on screen, m,

r = actual length of reference line, m,

R = reference line projected on screen, m, and

t_c = exposure time of frame observed, s.

The second method of analysis was based on the distance a particle travels in successive frames. The basic concept is the same as the first method; however, it was found to give more accurate results. The particle velocity is determined using

$$V = n \frac{r}{R} S \tag{2}$$

where

n = length traveled by particle between two successive frames, m

S = film speed (local quantity), m/s, and

r,R = same as in Eq. (1).

In practice, a combination of the two methods was used and checked against each other.

A certain amount of skill is required to obtain high quality movies of the particle trajectories, and several precautions are required. First, an optically black background inside test section wall is required and the specially designed front lighted system was found to give excellent results. Second, the camera speed must be well matched to the particle speed

otherwise the measured streaks will either be toosmall, making
their measurement inaccurate, or too large resulting in frame
size problems. In addition, the number of particles present
in each frame is important.

Erosion Rate Test

Material erosion rate data was obtained for INCO 718,
Ti 6-4, 2024 AL and DSR 150. It is well known from previous
testing that particle velocity, particle impingement angle,
aerodynamic effects, and the material sample temperature
strongly influence the erosion rate. These parameters were
varied in the present test program. Parameters of second
importance, such as particle size, sample size, particle
concentration, and sample heat treat conditions were held
constant in this investigation. In some cases, the heat treat
condition was varied.

The material erosion was determined from the weight of the
19.0 x 25.4 mm specimen before and after testing. These specimen
were polished prior to testing. In the case of heat treatable
materials, such as INCO 718, some samples were heat treated
or aged to increase their hardness and strength while some
samples were left in the as received condition.

Erosion rate data was obtained for varied parameters as
follows. The impingement angle was varied from 15° to 90°
with the majority of the data obtained at 20°, 25°, 45°, 60°
and 90°. The particle impingement velocity was varied from
90 ft/sec to 1,000 ft/sec and the target temperature from ambient
to 1,500°F. The detailed test matrix of erosion rate data is
given in Table 4.

TABLE 4 - MATERIAL EROSION RATE TEST SUMMARY

Target Material	No. of Test Points	Target Temp. °C (°F)	Impingement Angle, °	Impingement Velocity m/s (ft/sec)	
Ti 6-4	111	Ambient to 771 (1420)	15, 20, 25, 30, 45, 60, 90°	27 to 320	(89) (1050)
INCO 718	69	Ambient to 810 (1490)	20, 25, 30, 45, 60, 90°	56.4 to 273	(185) (895)
2024 AL	76	Ambient to 521 (970)	15, 20, 25, 30, 45, 60, 90	49.1 to 267	(161) (876)
DSR 150	2	Ambient	45, 90	76.2	(250)
Lead	1	Ambient	45	76.2	(250)
Berillium	1	Ambient	45	76.2	(250)

Particle Rebound Geometry and Parameters

Particle rebound characteristics are important due to their effect on erosion patterns and erosion rates. Evaluation or prediction of erosion patterns in a turbomachine is complex. The first step is to calculate the particle trajectories through the machine where a detailed knowledge of the particles rebound characteristics is needed. This means the velocities and the angles restitution ratios. The restitution ratio is defined as the ratio between the particle relative velocities after and before collision. With the velocity and angle of attack restitution ratios, it is possible to perform the trajectory calculations from one stage to the other through the machine. In addition, particle rebound characteristics are useful in the prediction of erosion rate. This is because the particle rebound characteristics are a measure of the work inputted by the particles into the target material.

The particle rebound characteristics are statistical, in nature. The rough target surface and the irregular particles result in particles rebound over a wide range of angle and velocity.

The present investigation deals with the measurement of the distribution of the rebound characteristics. The measurement and prediction of rebound characteristics deal with single impact events. The distributions are then representative of a set of these events. The geometry of a single impact is described below.

In the investigation of particle rebound characteristics, the geometry of both the impact and rebound must be understood and the pertinent rebound parameters defined. Figure 5 depicts a single particle impact and rebound. In this case, a particle impacts at velocity V_1 and angle β_1. The coordinate system is defined with the Z axis normal to the target surface at the impact point and the trajectory of the impinging particle is in the XZ plane. The impingement velocity is, therefore composed

14

of a component normal to the impacted surface V_{N_1} and one tangential to the surface V_{T_1}. The particle rebounds at a velocity V_2 and angle β_2. This rebound is not necessarily in the plane of the impact velocity as indicated by angle α_2. The rebound velocity has a component normal to the impacting surface V_{N_2} and one tangential to the surface V_{T_2}. The component of the rebound velocity tangential to the impact surface V_{T_2} is further reduced to a component in the plane of the impingement velocity $V_{T_{2M}}$ and an out of plane component $V_{T_{2Y}}$. The usefulness of these parameters is described below.

The particle rebound geometry shown in Fig. 5 depicts an actual particle impact event. Measurement of these events was made using high speed photography as described previously. During these measurements the high speed movie camera was aligned normal to the plane of the impacting particles as shown in Fig. 6. As a consequence, the particle rebound characteristics were measured only as projections in the XZ plane, i.e., out of plane rebound velocity components were not measured. As Fig. 5 indicates, however, the particle rebound velocity will generally have out of plane components.

The measured particle impingement and rebound parameters are the impingement angle (β_1), velocity (V_1), plus the rebound angle (β_{2M}) and velocity (V_{2M}). From these measured values, the normal and tangential components V_{N1}, V_{T1}, V_{N2M} were computed directly. Based on the measured and directly calculated impingement and rebound angles and velocities, the pertinent restitution ratios were defined as follows:

$$\text{Velocity Restitution Ratio} = e_v = \frac{V_{2M}}{V_1} \tag{3}$$

$$\text{Tangential Restitution Ratio} = e_T = \frac{V_{T_{2M}}}{V_{T_1}} \tag{4}$$

15

$$\text{Normal Restitution Ratio} = e_N = \frac{V_{N_{2M}}}{V_{N_1}} \qquad (5)$$

$$\text{Angle Restitution Ratio} = e_\beta = \frac{\beta_{2M}}{\beta_1} \qquad (6)$$

Evidence that the out of plane tangential rebound velocity $V_{T_{2Y}}$ as depicted in Fig. 5 exists for all impingement angles tested is manifested in the observed erosion of the test section window. The windows showed significant erosion in the vicinity of the target surface for all tested incidence angles. This erosion was severe enough to require replacement of the window between test points. The most severe window erosion occurred at an impingement angle of 90° and became less severe as the impingement angle decreased.

EXPERIMENTAL RESULTS AND DISCUSSION

Particle Rebound Experimental Results

General Description:

Particle rebound restitution ratios have been obtained from the experimentally controlled parameters such as particle impingement angle, target temperature, target material, particle impingement velocity and target material grain orientation. In addition, relationships among the rebound parameters were investigated. Also, the work and impulse into the target material due to the particle impingement was evaluated based on the measured particle rebound characteristics, i.e., rebound restitution ratios.

Effect of Impingement and Rebound Angle on Particle Rebound Characteristics:

The effect of particle impingement angle on rebound characteristics was considered due to its importance as determined in previous test experiments. Also, impingement angle strongly affects erosion rate results as measured in the present erosion testing and that of previous investigators. The measured absolute average particle rebound angle is shown relative to the particle impingement angle for the various target materials in Figs. 7 through 10. The significance of utilizing the absolute average rebound velocity is explained later in this section. Similarly, the effect of impingement angle on each of the particle rebound restitution ratios is presented in Figs. 11 through 13. In the above figures, no attempt is made to distinguish velocity, material or temperature effects which are described in subsequent sections.

From Figs. 7 through 10, it can be seen that the particle rebound angle is strongly influenced by the impingement angle. For each target material, the rebound angle increases from an assumed zero value at a zero impingement angle to appreoximately 67° at a 90° impingement angle.

17

Similarly, as depicted in Figs. 11 through 13, the impinge-
ment angle has a strong influence on each of the important
particle restitution ratios. The standard deviation for the
rebound angle, velocity and tangential velocity restitution
ratios for all materials tested are shown in Figs. 14 through 16
as a function of impingement angle. The angle restitution
ratio deviation shows a very significant relationship with
impingement angle, whereas the velocity restitution ratios
standard deviation shows only a mild relationship with impinge-
ment angle. None of the standard deviations were influenced
by target temperature or material.

Figure 17 shows the measured rebound angle density distri-
bution for 25, 45, 60 and 90 degree impingement angles. These
plots represent the probability that a particle will rebound
at a particular angle relative to the impingement angle.
Each curve on Fig. 17 represents the rebound probability
distribution or function for each impingement angle measured.
The prabability function in polar coordinates is:

$$\int_{0}^{\pi} f(\theta) \, d\theta = 1 \tag{7}$$

Therefore the area under each curve is equal to unity, i.e.,
the probability that the rebound angle falls within the distri-
bution is unity. These curves can be used in the prediction
of particle rebound characteristics.

Several observations can be made concerning the rebound
angle characteristics exhibited in Fig. 17. At an impingement
angle of 90°, the significance of the average and absolute
average rebound angle becomes apparent. The angle of highest
probability for the rebound angle following a 90° impingement
angle is at the absolute average rebound angle. However, the
center of the probability distribution for the rebound angle is
at the average value of 90°. At a 60° impingement angle, the
difference between the average and absolute rebound angle has
become insignificant and remains so as the impingement angle is
further reduced. Another observation is that the probability

18

function is braod at an impingement angle of 90° encompassing a broad range of rebound angles. As the impingement angle is reduced, the probability distribution becomes more peaked, encompassing a smaller range of rebound angles (see Fig. 17).

In the restitution ratio plots presented above, the velocity restitution ratios were assumed to be independent of the angle restitution ratio. To test this hypothesis the velocity restitution ratio was plotted versus the particle rebound angle for several test points. One of these is shown in Fig. 18. From this plot, the rebound velocity parameter seems to be relatively independent of rebound angle.

Effect of Target Temperature on Particle Rebound Characteristics:

Erosion rate data from this test program indicates that erosion rate can increase abruptly at elevated target temperature. Also, the erosion rate equation presented in reference [1] utilizes tangential velocity restitution ratio as part of the functional relationship affecting erosion. Based on the above, the effect of target temperature on particle rebound restitution ratios was examined as shown in Figs. 19 through 23. The data indicates no significant tendency for the velocity or angle restitution ratios to vary with increasing target temperatures for all materials tested. The angle restitution ratio appears insensitive to target temperature. Additionally, the target materials are differentiated on these plots and indicate insensitivity of rebound characteristics to target material as well.

Effect of Target Material on Particle Rebound Characteristics:

Significantly different erosion rates were exhibited among the materials tested. Therefore, the possibility of similar variations in particle rebound characteristics relative to target material was investigated. The average values of the important restitution ratios are shown as a function of the three target materials 2024 AL, Ti 6-4 and INCO 718 on Fig. 24. The comparison of rebound characteristics for the different materials is made at particle impingement angles of 25, 45 and 90°. With the

19

exception of the tangential restitution ratio, no consistent
or significant variation among the three materials is evident.
The variations which are present may represent primary data
scatter even for the tangential restitution ratio.

Effect of Velocity on Rebound Characteristics

Erosion rate has been shown to be a strong function of
particle impingement velocity in the present test program. In
addition, tangential restitution ratio has been used as a
parameter in an erosion rate prediction equation[1]. For
these reasons, the effect of particle velocity on particle
rebound characteristics was considered. Tangential and normal
velocity restitution ratios were compared with tangential and
normal impingement velocity in Figs. 25 and 26, respectively.
In each case, impingement angle was held constant.

The normal restitution ratio is strongly influenced by
impingement angle as shown in Fig. 25. At impingement angles
of 45° or greater, the normal restitution ratio measurements
indicate normal particle impingement velocity has little effect
on normal restitution ratio. At an impingement angle of 25°
the normal restitution ratio increases with decreasing normal
particle impingement velocity. Since the magnitude of the
normal velocity is dependent to some extent on the impingement
angle in this test, i.e., the lower impingement angles resulted
in lower normal impingement velocities, it is possible, but not
determinable from the data, that the same increase in restitution
ratio may occur at the higher impingement angles at low normal
impingement velocities.

The tangential restitution ratio showed insensitivity to
the tangential impingement velocity and impingement angle. Note
that the tangential restitution ratios are higher than the
normal restitution ratios for the range of velocities measured,
but tend towards each other at low velocities. This may indicate
that the tangential restitution ratio is not affected by plastic
deformation, whereas the normal restitution ratio is strongly
influenced by plastic deformation.

20

Statistical Nature of Particle Rebound Characteristics

The statistical nature of the particle rebound character-
istics along with their average trends are displayed graphically
on Figs. 27 through 30. Each figure represent the distribution
of an important rebound restitution ratio described at each of
the measurement impingement angles. Displayed in this manner,
the nature of the rebound characteristics can be visualized.
Each distribution represents the entire data base at each
impingement angle. As shown here, the rebound characteristics
are strongly related to the impingement angle. The majority
of the distributions are roughly a bell-shaped normal distribution.
The basic exception to this is the two hump distributions for
rebound angles at and near an impingement angle of 90°. This
hump distribution is caused by the rebound angles distributing
in both the first and second quandrants of the measurement
planes. The average value for each of the distributions is
represented by the solid curve on each figure. The equation
for each curve is included on each figure. The dotted lines
show the standard deviation for each restitution ratio.

Effect of Restitution Ratio on Impulse and Work Imparted to the Target Material:

In an effort to understand the relationship between the
rebound restitution ratio and erosion rate, the impulse and
work imparted to the target material was evaluated based on the
measured tangential and normal rebound restitution ratios
as described below:

For Tangential Direction:

Impulse: $\quad I_T = m_1 V_1 \cos\beta_1 (1 - e_T)$ $\hfill (8)$

Work: $\quad W_T = m_1 V_1^2 \cos^2\beta_1 (1 - e_T^2)$ $\hfill (9)$

For Normal Direction:

Impulse: $\quad I_N = m_1 V_1 \sin\beta_1 (1 + e_N)$ $\hspace{2cm}$ (10)

Work: $\quad\quad W_N = m_1 V_1^2 \sin^2\beta (1 - e_N^2)$ $\hspace{2cm}$ (11)

where m_1 equals particle mass. The work and impulse imparted
to the target material during an average collision are plotted
in Figs. 31 and 32. In Fig. 31 the work and impulse imparted
in the direction tangential to the target surface is described
as a function of impingement angle. Figure 32 represents a
similar description of work and impulse in the normal directions.

Several interesting observations are apparent from the
work and impulse relationship for the tangential and normal
directions. First, the tangential work and impulse functions
reach a maximum at the impingement angle of maximum erosion.
Also the tangential function has a zero value at a zero
impingement angle with a corresponding zero erosion rate.

The normal impulse and work function on the other hand
closely follows the trend of brittle erosion rate or the erosion
rate attributable to the normal impact. Note also that the
impulse function factor for the normal impact is greater than
the work function factor for normal impact, while the reverse
is true for the tangential impact. In addition, the impulse
factor for the normal impact is in general greater than that for
the tangential impact. This is caused by the particle changing
direction in the normal impact, while the particles do not
change tangential direction.

Erosion Rate Equations

A multiple regression analysis was performed using the
erosion rate data accumulated in this program to obtain semi-
empirical erosion rate equations for 2024 AL, Ti 6-4 and INCO 718
materials. The equations are semi-empirical, based on theoretical

considerations and knowledge of important parameters such as
the work input into the target material due to the particle
impacts and the particle restitution ratios. The results are
present below in terms of volumetric erosion rate (ε_V). The
mass erosion rate (ε_G) can be determined using the following
relationship:

$$\varepsilon_G = \rho\ \varepsilon_V \tag{12}$$

2024 AL

$$\varepsilon_V = 0.1076^{-4}[(\frac{Y_{SRT}}{Y_S})^{0.47} + (\frac{Y_S}{Y_{SRT}}) - 1]\{(\frac{V_1}{100})^{2.9}(1-e_T^2)\cos^2\beta_1$$

$$+ 0.0422(\frac{V_1}{100})^4(1-e_N^2)\sin^2\beta_1\} \tag{13}$$

Ti 6-4

$$\varepsilon_V = 0.149^{-4}[(\frac{Y_{SRT}}{Y_S})^{0.28} + (\frac{Y_S}{Y_{SRT}}) - 1]\{(\frac{V_1}{100})^{2.4}(1-e_T^2)\cos^2\beta_1$$

$$+ 0.101(\frac{V_1}{100})^{2.9}(1-e_N^2)\sin^2\beta_1\} \tag{14}$$

INCO 718

$$\varepsilon_V = 0.055^{-4}[(\frac{Y_{SRT}}{Y_S})^{2.9} + (\frac{Y_S}{Y_{SRT}}) - 1]\{(\frac{V_1}{100})^{2.8}(1-e_T^2)\cos^2\beta_1$$

$$- 0.114(\frac{V_1}{100})^3(1-e_N^2)\sin^2\beta_1\} \tag{15}$$

where ε_V = volumetric erosion rate, cm3/gm.

Y_{SRT} = material yield strength at ambient temperature.

Y_S = material yield strength at operating temperature.

EXPERIMENTAL EROSION RATE RESULTS AND DISCUSSION

Effect of Particle Velocity

Particle velocity was found to have a powerful effect on erosion rates. In all cases investigated, the erosion rate was shown to be proportional to the particle velocity taken to a constant power. This is similar to the results found by earlier investigators. Erosion rate versus particle velocity data for Ti 6-4 is displayed in Figs. 33 through 36. On each figure, the volumetric erosion rate is plotted versus particle velocity for different sample temperatures. Each figure represents a different particle impingement angle. For Ti 6-4, erosion rate is shown to be proportional to the particle velocity to the n power when n represents the slope of the straight lines on these figures. The range of n is depending on the angle of attack and the sample temperature.

Erosion rate data for INCO 718 is similarly plotted on Figs. 37 through 40. Similar to Ti 6-4, the erosion rate was found to be proportional to particle velocity taken to a power with the exponent, a function of both sample temperature and impingement angle.

Both materials tested exhibited similar characteristics with the velocity exponent tending to increase with increasing impingement angle and decrease with increasing the sample temperature. It is interesting to note the wide range of the exponent values for any one material. This variation has been shown to be related to the particle velocity restitution ratio in reference 1. Apparently, both increases in impingement angle and sample temperature effect the restitution ratio and this effects the erosion rate.

Effect of Sample Temperature

The erosion rate versus the sample temperature is presented in Figures 41 and 42 for the two materials being considered. The results in these figures are for a particle velocity of 500 ft/sec, and are cross plotted from the erosion rate versus

particle velocity curves presented earlier.

Erosion rate versus sample temperature shows a slightly different trend for Ti 6-4 as shown in Fig. 41. The erosion rate increases slowly as the sample temperature is increased from room temperature to 800°F for 25 and 45 degrees particle impingement angles. As the sample temperature is increased above 800°F, the erosion rate increases rapidly. Erosion rate shows a much slower rate of increase for Ti 6-4 at an impingement angle of 90° as sample temperature is increased. Inspection of Fig. 42 shows that the erosion rate for INCO 718 increases slowly or stays constant up to a sample temperature around 900°F, then increases abruptly as the sample temperature increases. This trend is independent of the impingement angle for INCO 718.

Effect of Particle Impingement Angle

It is well known that erosion rate is a function of particle impingement angle. For ductile materials, erosion rate increases from zero at a zero degree impingement angle to a maximum. After reaching a maximum, the erosion rate decreases with increasing impingement angle to a minimum value at 90° impingement angle.

The plots of erosion rate versus particle impingement angle presented in this paper are cross plotted from the erosion rate versus material sample temperature presented earlier. These impingement angle curves are for a particle velocity of 500 ft/sec in all cases. Also, each plot of erosion rate versus impingement angle is for a constant sample temperature. The erosion rates versus the particle impingement angles for different sample temperatures are presented in Figs. 43 and 44 for Ti 6-4 and INCO 718 correspondingly. The erosion rate is a maximum for Ti 6-4 at an impingement angle of 30 degrees and for the INCO 718 at 35 degrees.

Effect of Sample Material

The erosion rate results presented previously show significantly different levels for the two different materials considered. An attempt was made to determine a parameter which would account for the different material properties. The erosion rate versus the sample temperature for a particle velocity of 500 ft/sec and impingement angle of 25° is presented for the two materials in Fig. 45. From this figure, it becomes apparent that the erosion rate behaves in a similar fashion for each material. The level of erosion and the temperature where the erosion rate increases rapidly is different for each material.

In order to improve the correlation of erosion rate with the sample temperature and remove the material effect, the erosion rate was plotted versus the normalized sample temperature. In Fig. 46, the sample temperature is normalized using sample melting temperature. This plot does not seem a significant improvement compared with sample temperature (Fig.   ). In addition, the sample material annealed temperature was used as the normalizing temperature, and is shown in Fig. 47. This normalization of the data gives the best correlation of the data for both materials.

Figure 47 shows that the material erosion rate may be related to the annealed temperature, and that the erosion rate increases abruptly as the material sample temperature approaches the annealed temperature. This could indicate that the material erosion rate increases rapidly as the yield strength decreases rapidly near the annealed temperature. This would support the contention that material erosion rate is related to material yield strength.

26

CONCLUSIONS

The major conclusions are derived from the test results
and analyses as follows:

1. Particle rebound characteristics are generally influenced
   by impingement angle.

2. Particle rebound characteristics are not affected
   significantly by target material or temperature
   for common superalloys.

3. The restitution ratios at low impingement angle is
   generally not affected by target material or
   temperature.

4. Tangential restitution ratio is insensitive to
   tangential impingement velocity.

5. Normal restitution ratio is insensitive to normal
   impingement velocity, except at low velocities or
   low impingement angles.

6. Work and impulse imparted to the target material by
   by the impinging particles are strong functions of
   impingement angle and represent the angle effect on
   erosion rate.

7. Two significant conclusions can be drawn from the data
   presented. Erosion rate remains relatively constant
   for INCO 718 and Ti 6-4 from room temperature up to a
   temperature unique for each material, then increases
   rapidly with material temperature. Also, the impingement
   angle at which maximum erosion occurs for each material
   is independent of the material sample temperature.
   Additionally, the velocity exponent varies considerably
   with changes in both the impingement angle and the
   material sample temperature. Ultimately, the date pre-
   sented here will be used to predict the erosion in jet
   engine compressors. Use of only room temperature data
   could yield erroneous results due to the changes in
   the material erosion rate with increasing material
   temperature.

27

REFERENCES

1. Grant, G. and Tabakoff, W., "Erosion Prediction in Turbo-
    machinery Resulting from Environmental Solid Particles,"
    Journal of Aircraft, Vol. 12, May 1975, pp. 471-478.

2. Finnie, I., Wolak, J. and Kabil, Y., "Erosion of Metals by
    Solid Particles," Journal of Materials, Vol. 2, Sept. 1967,
    pp. 682-700.

3. Smeltzer, C.E., Gulden, M.E., McElmury, S.S. and Compton, W.A.,
    "Mechanisms of Sand Dust Erosion in Gas Turbine Engines,"
    USAAVLABS Tech. Report, August 1970.

4. Frass, A.P., "Survey of Turbine Bucket Erosion Deposits,
    and Corrosion," ASME Paper 75-GT-125, presented at the Gas
    Turbine Conference, Houston, Texas, March 2-6, 1975.

5. Finnie, I., "An Experimental Study on Erosion," Proceedings
    of the Society for Experimental Stress Analysis, Vol. 17,
    No. 2, pp. 65-70.

6. Tabakoff, W. and Hamed, A., "Aerodynamic Effects on Erosion
    in Turbomachinery," JSME and ASME Paper 70, 1977 Joint Gas
    Turbine Congress, Tokyo, Japan, May 22-27, 1977.

7. Tabakoff, W., and Wakeman, T., "Test Facility for Material
    Erosion at High Temperature," ASTM STP 664, American Society
    for Testing and Materials, 1979, pp. 123-135.
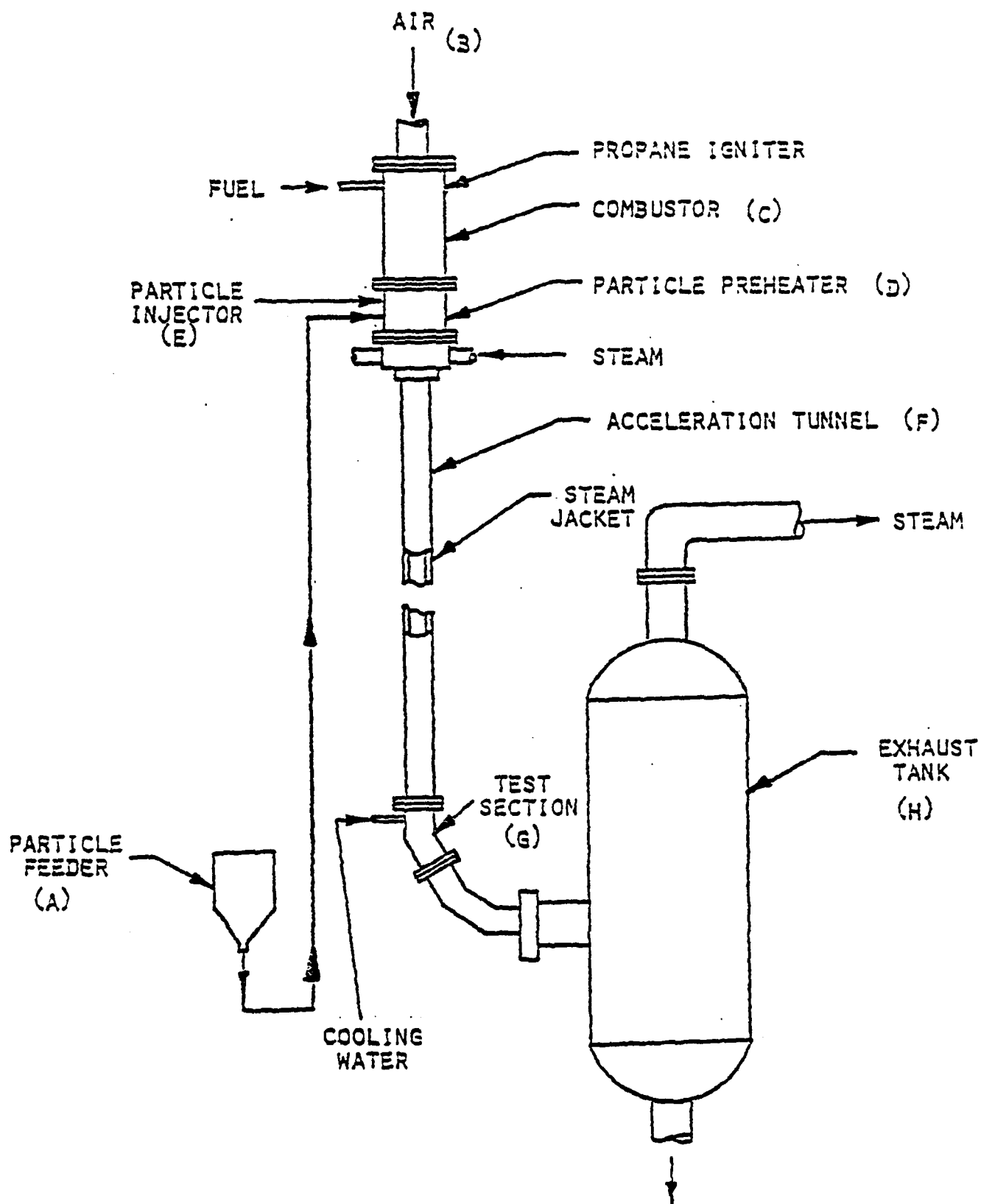
FIG. 1. SCHEMATIC OF ERCSION TEST FACILITY

29
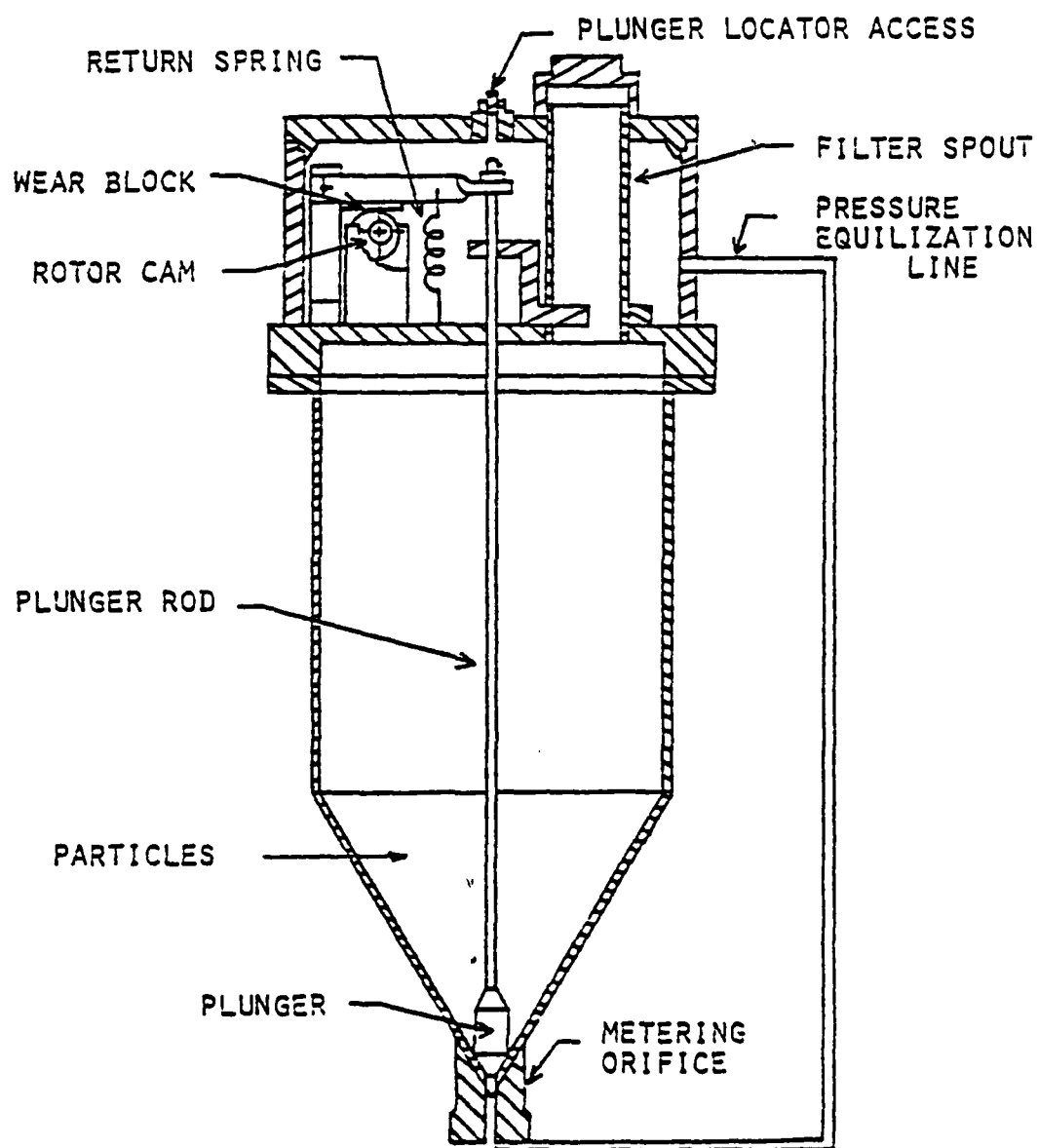
FIG. 2.   PARTICLE FEEDER ASSEMBLY
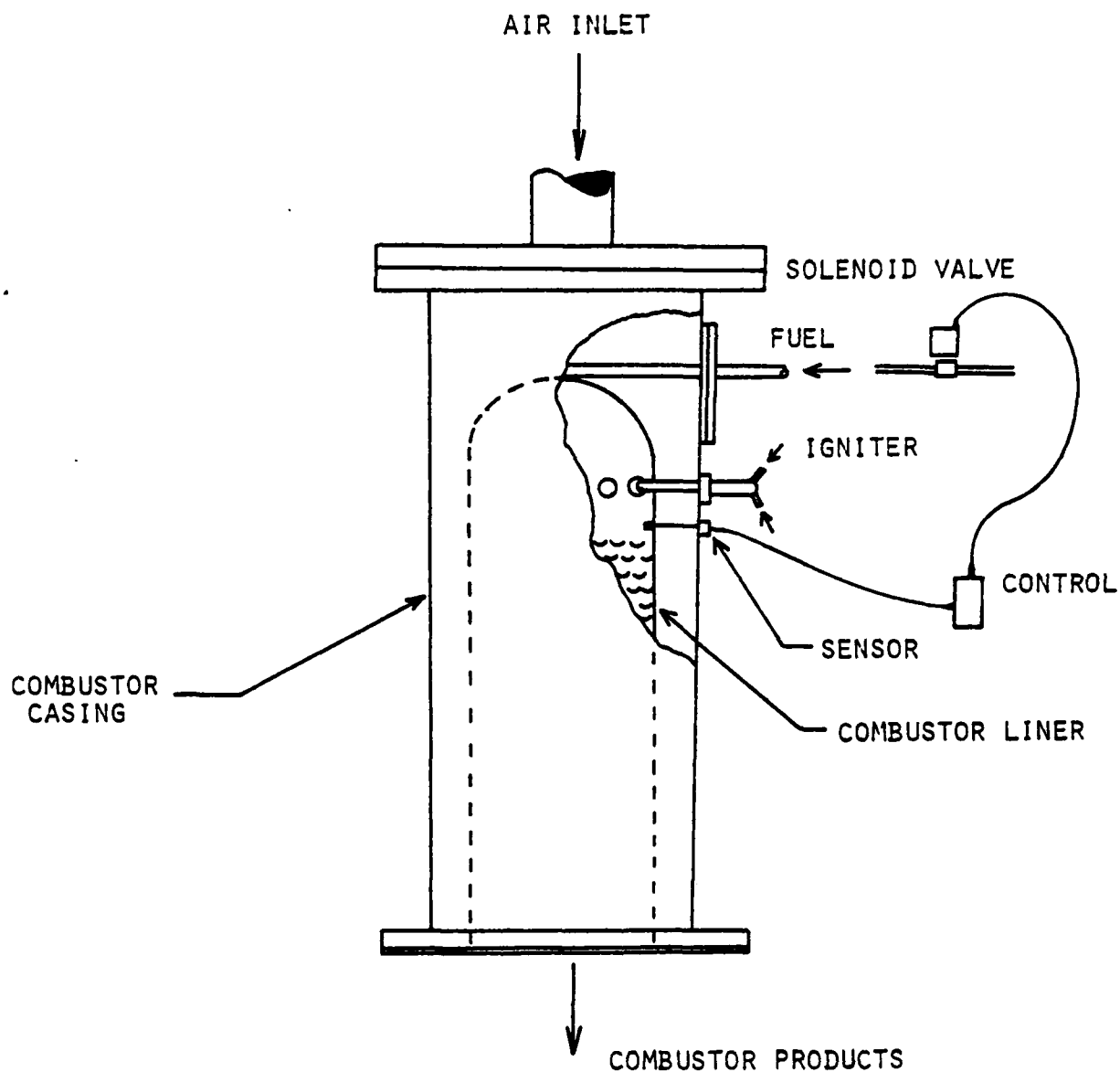
FIG. 3. COMBUSTION CHAMBER SCHEMATIC.

31
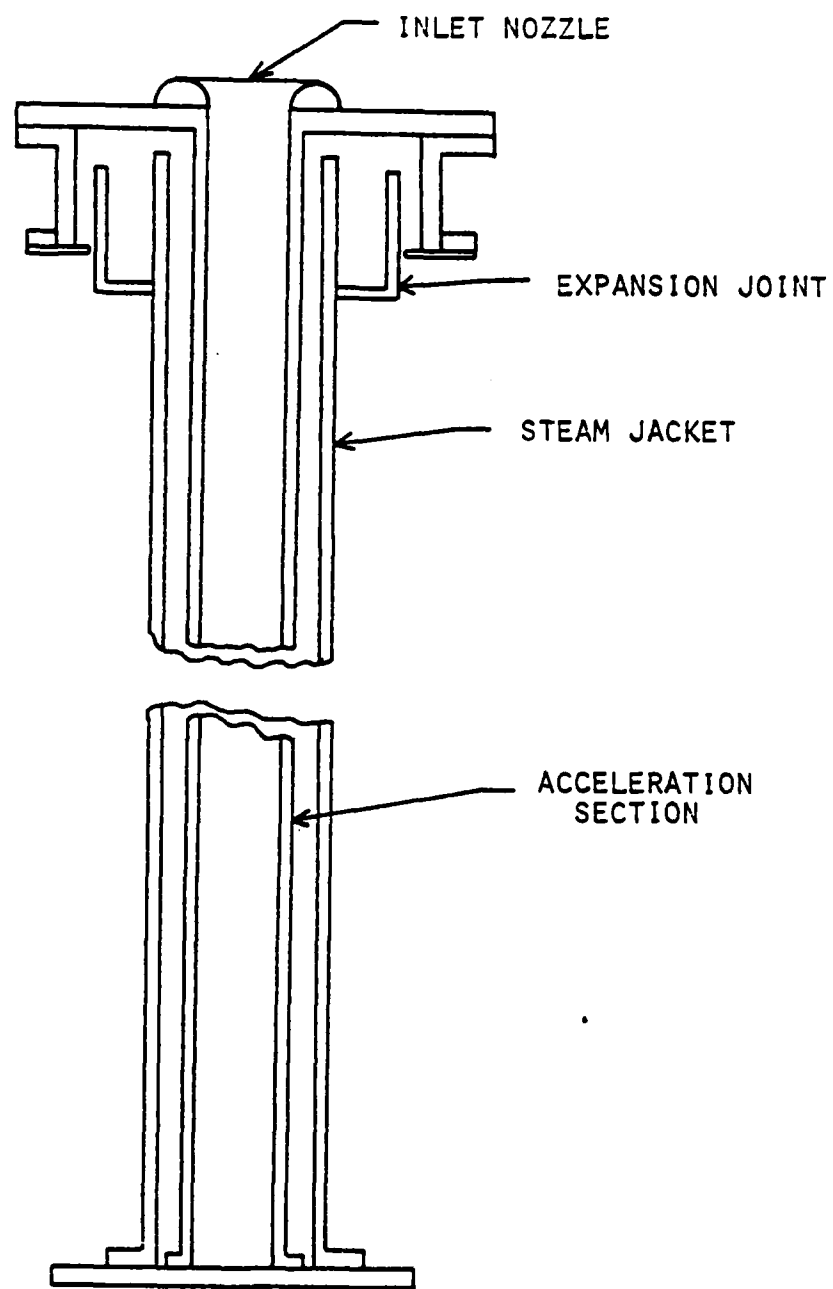
FIG. 4. SCHEMATIC OF THE ACCELERATION TUNNEL.
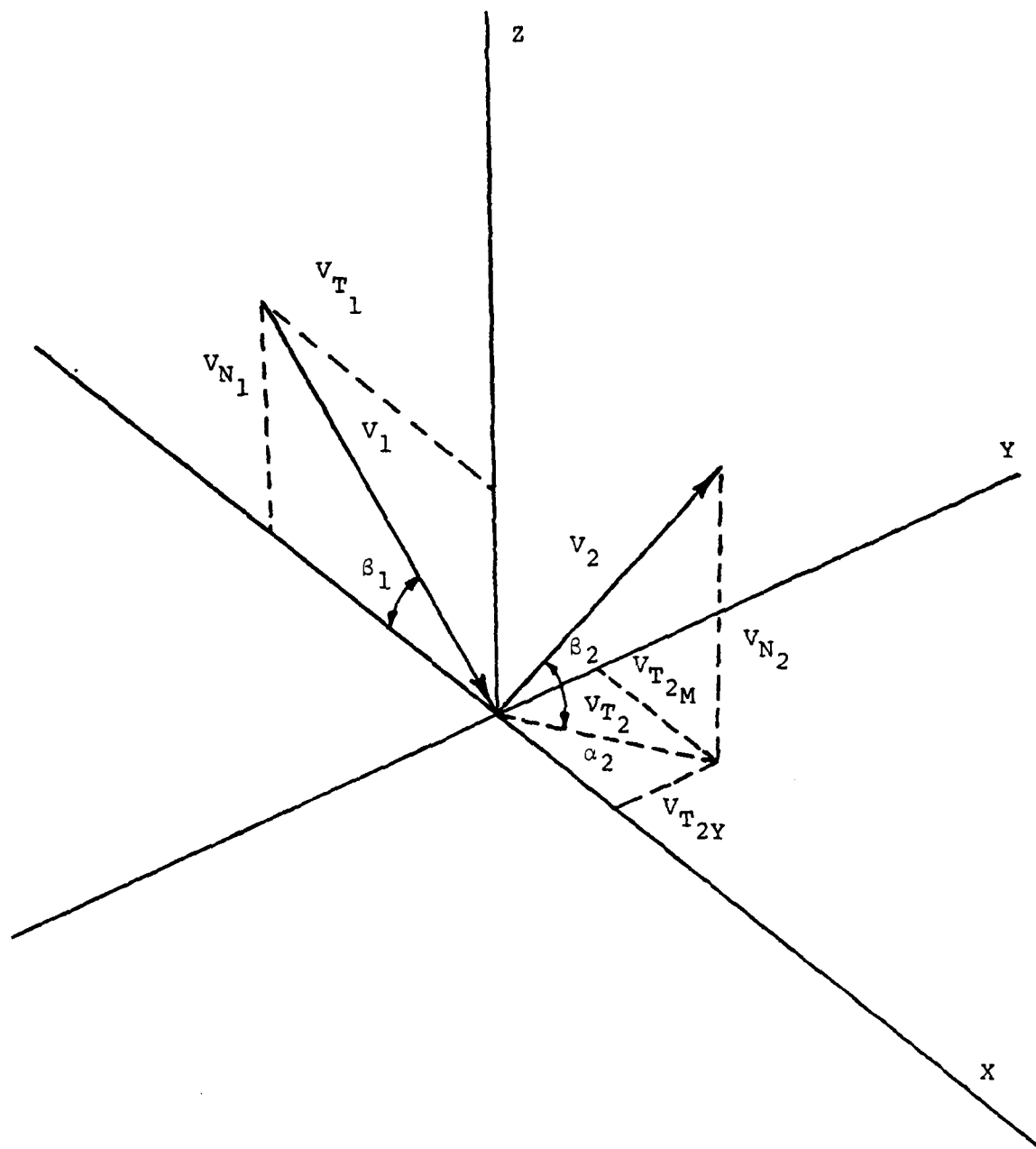
FIG. 5. PARTICLE IMPACT AND REBOUND GEOMETRY
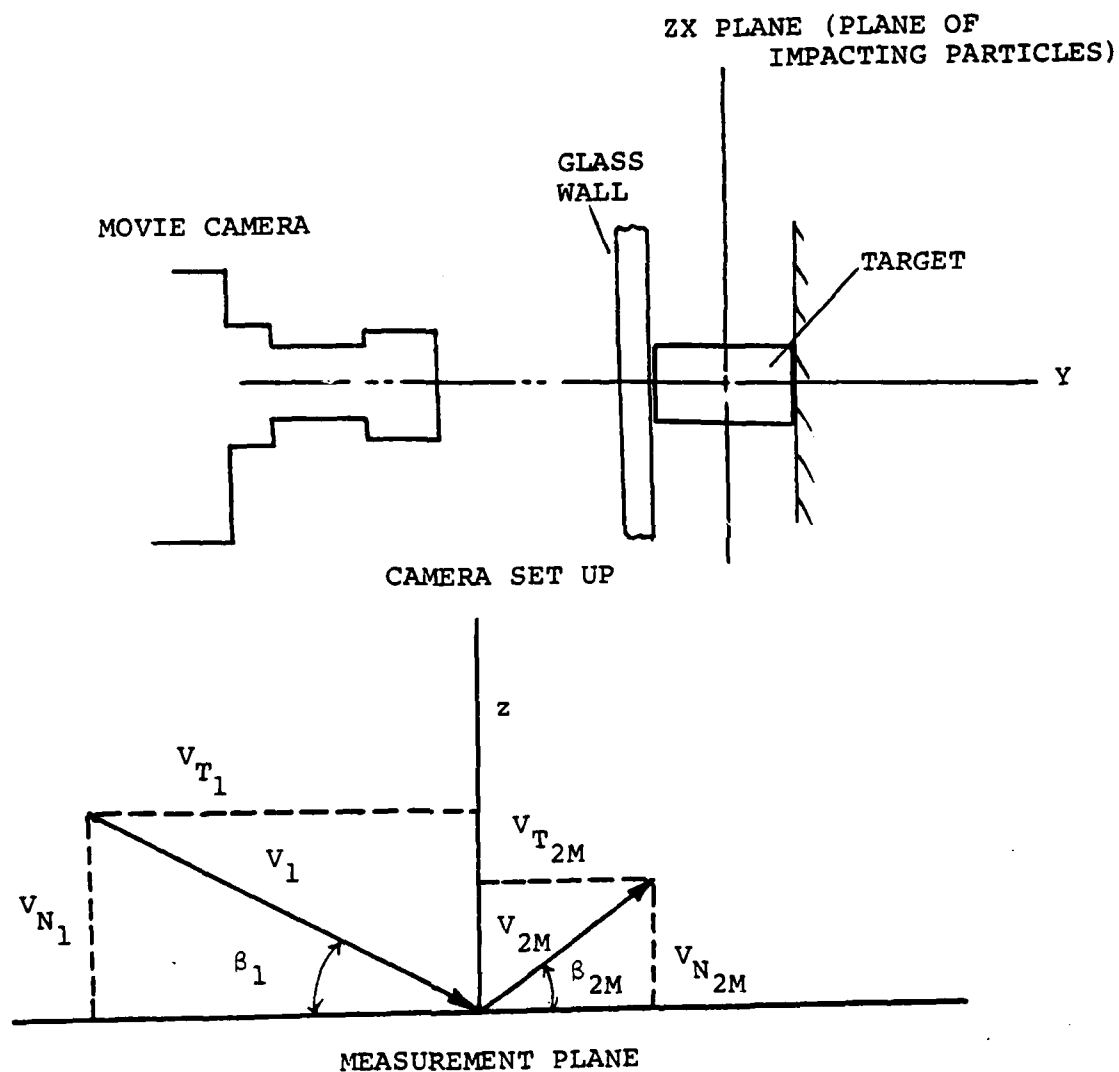
FIG. 6. CAMERA SET-UP AND MEASUREMENT PLANE USED IN THE MEASUREMENT AND INTERPRETATION OF PARTICLE REBOUND CHARACTERISTICS.

34
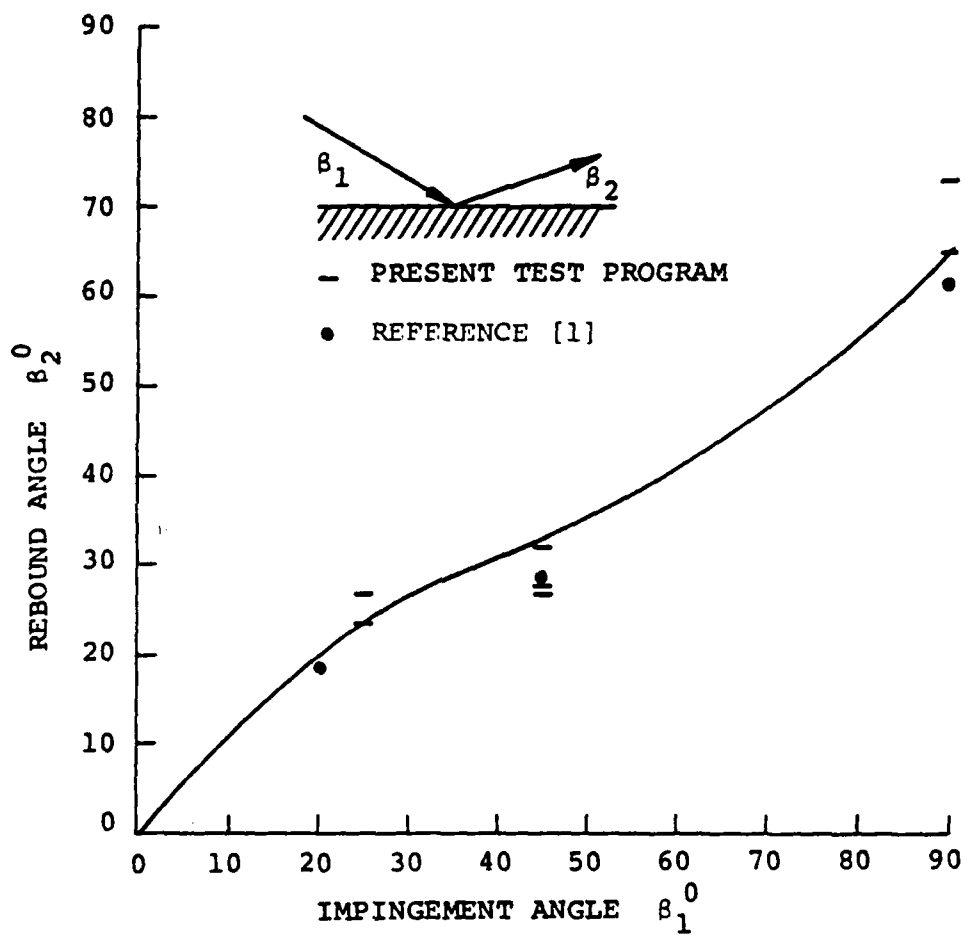
FIG.   7 .   COMPARISON OF MEASURED PARTICLE REBOUND ANGLE WITH
          IMPINGEMENT ANGLE FOR 2024 AL TARGET MATERIAL.

35
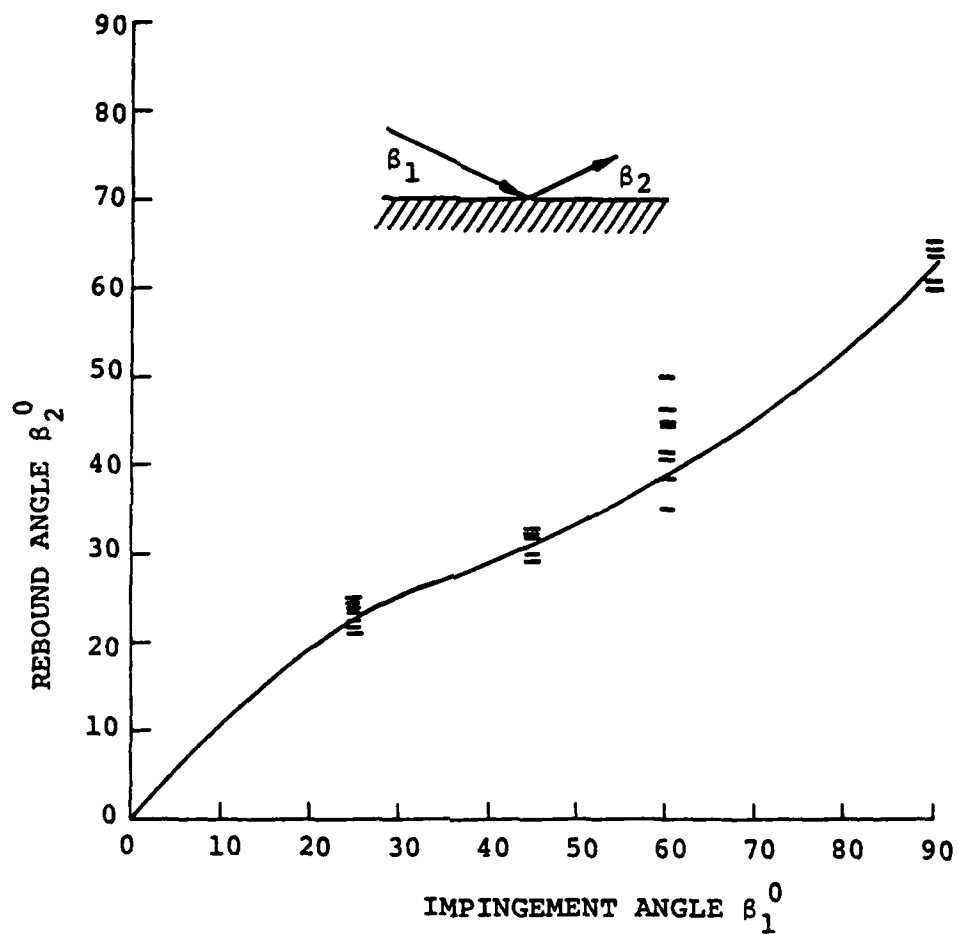
FIG. 8. COMPARISON OF MEASURED PARTICLE REBOUND ANGLE WITH
IMPINGEMENT ANGLE FOR Ti 6-4 TARGET MATERIAL.

36
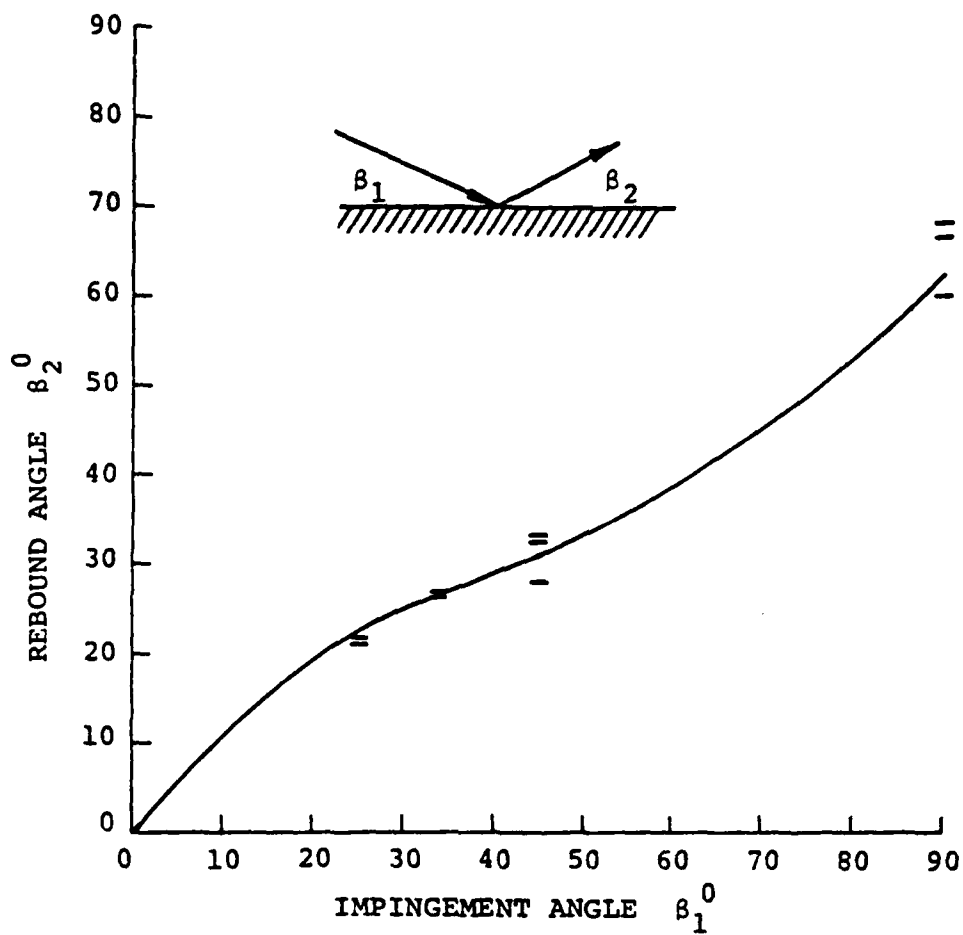
FIG. 9 . COMPARISON OF MEASURED PARTICLE REBOUND ANGLE WITH
IMPINGEMENT ANGLE FOR INCO 718 TARGET MATERIAL.
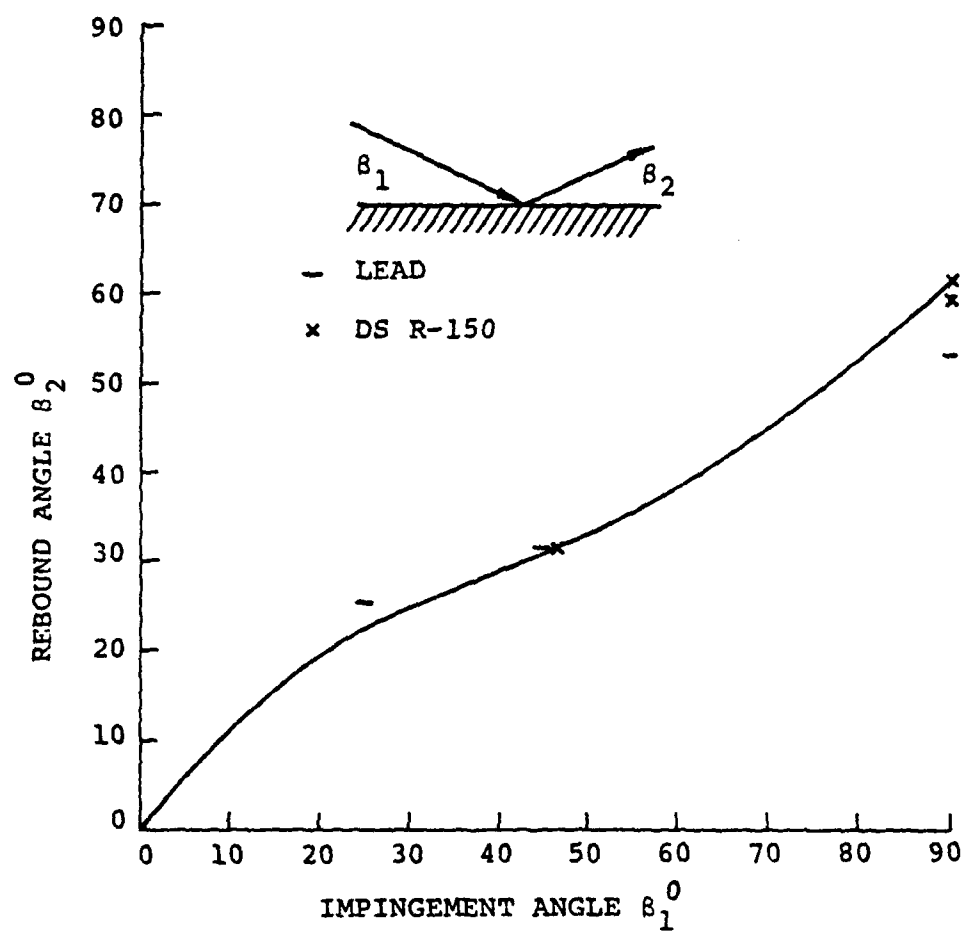
FIG. 10.   COMPARISON OF MEASURED PARTICLE REBOUND ANGLE
WITH IMPINGEMENT ANGLE FOR LEAD AND DS R150
TARGET MATERIAL.

38
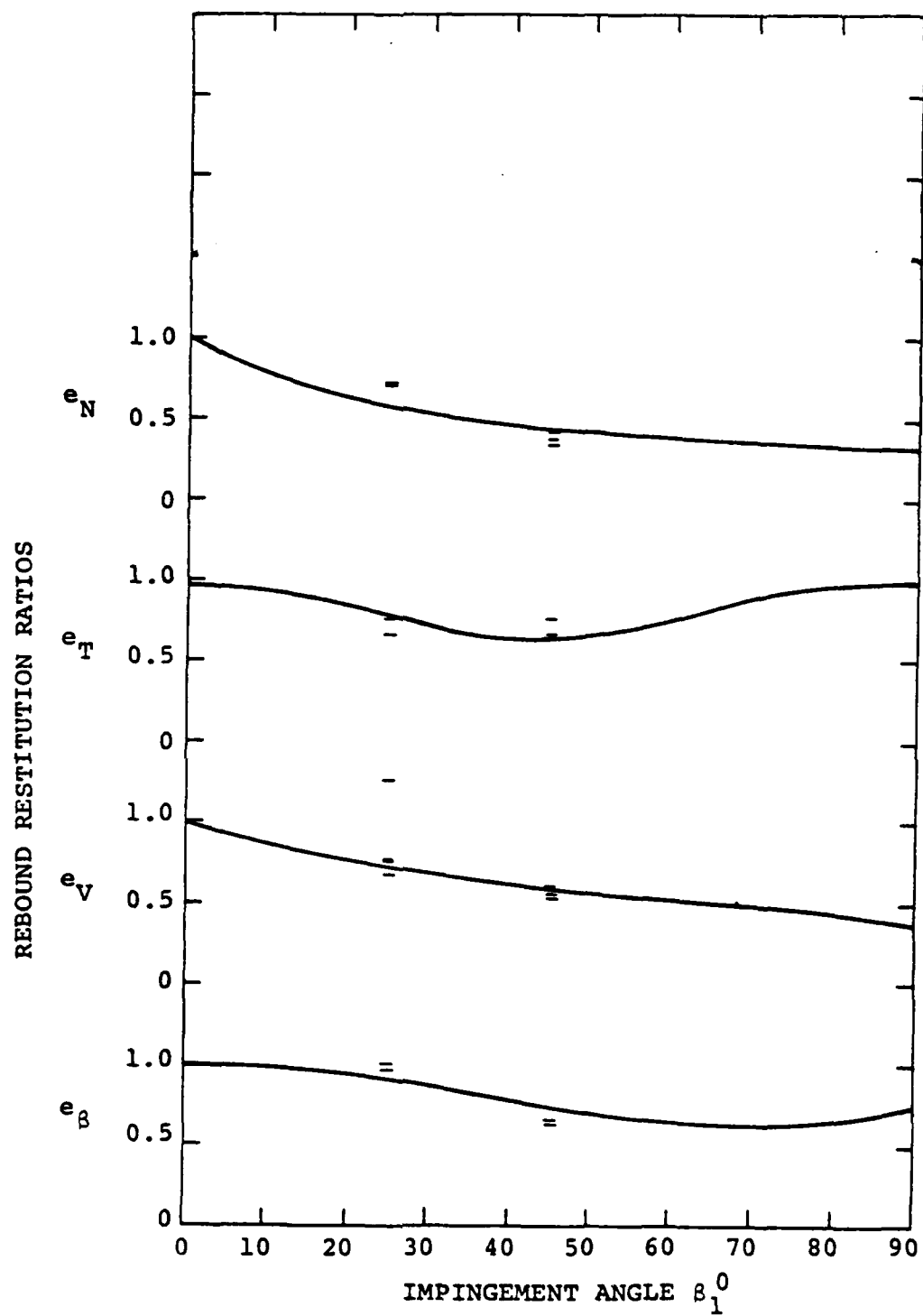
FIG. 11. COMPARISON OF MEASURED PARTICLE REBOUND RESTITUTION RATIOS
WITH IMPINGEMENT ANGLE FOR 2024 AL TARGET MATERIAL.

39
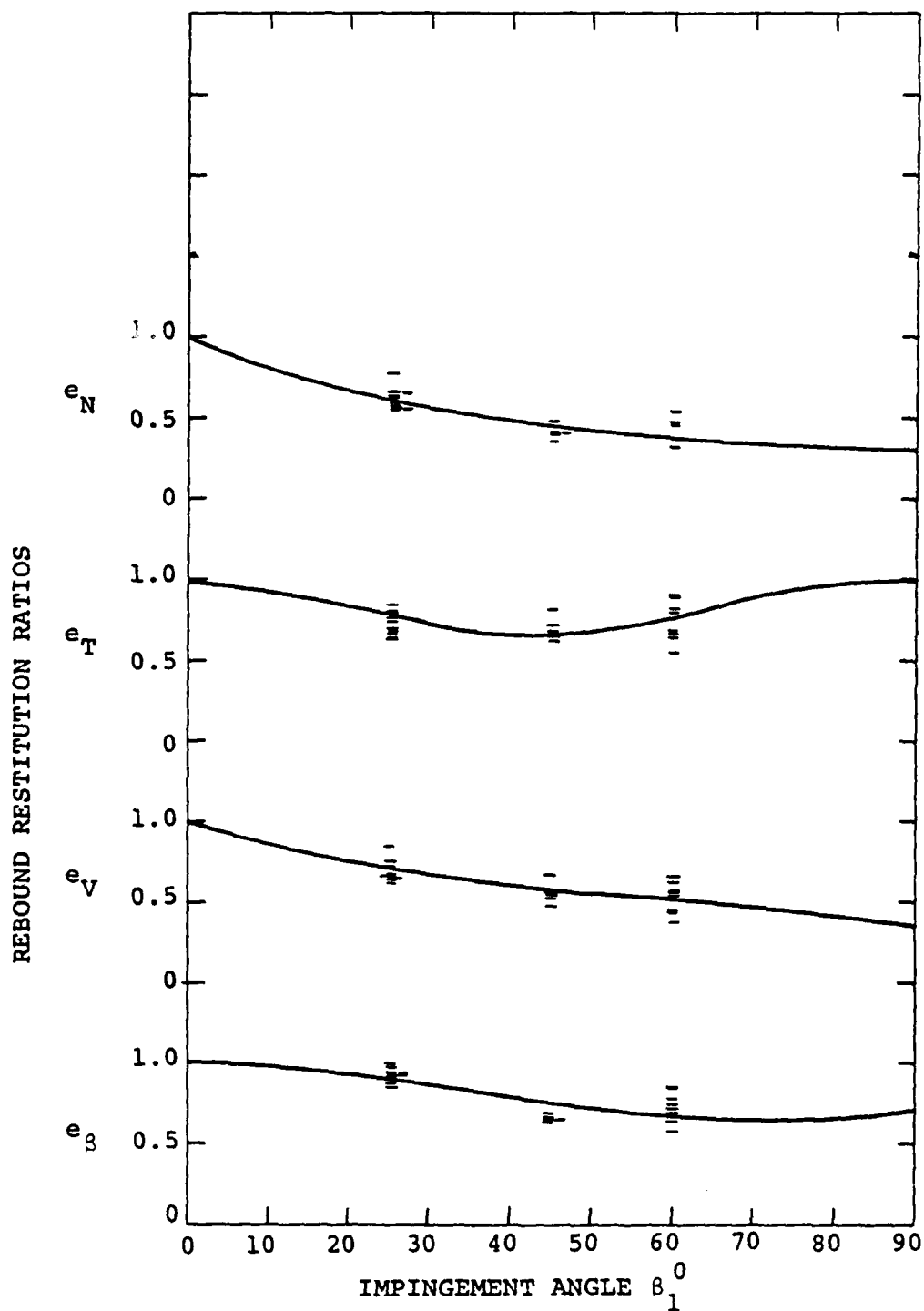
FIG. 12. COMPARISON OF MEASURED PARTICLE REBOUND RESTITUTION RATIOS
WITH IMPINGEMENT ANGLE FOR Ti 6-4 TARGET MATERIAL.

40
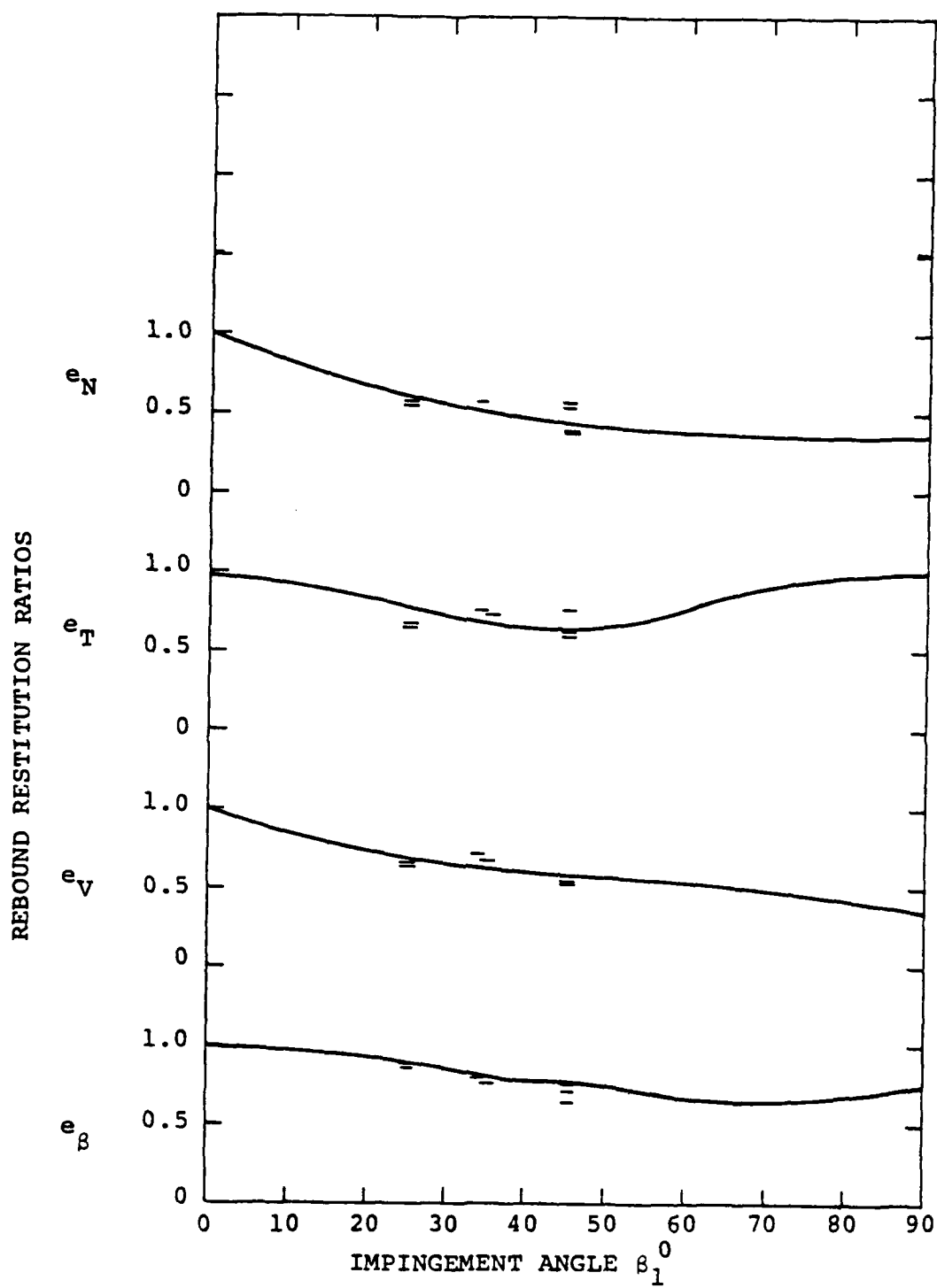
FIG. 13.   COMPARISON OF MEASURED PARTICLE REBOUND RESTITUTION RATIOS
WITH IMPINGEMENT ANGLE FOR INCO 718 TARGET MATERIAL.

41
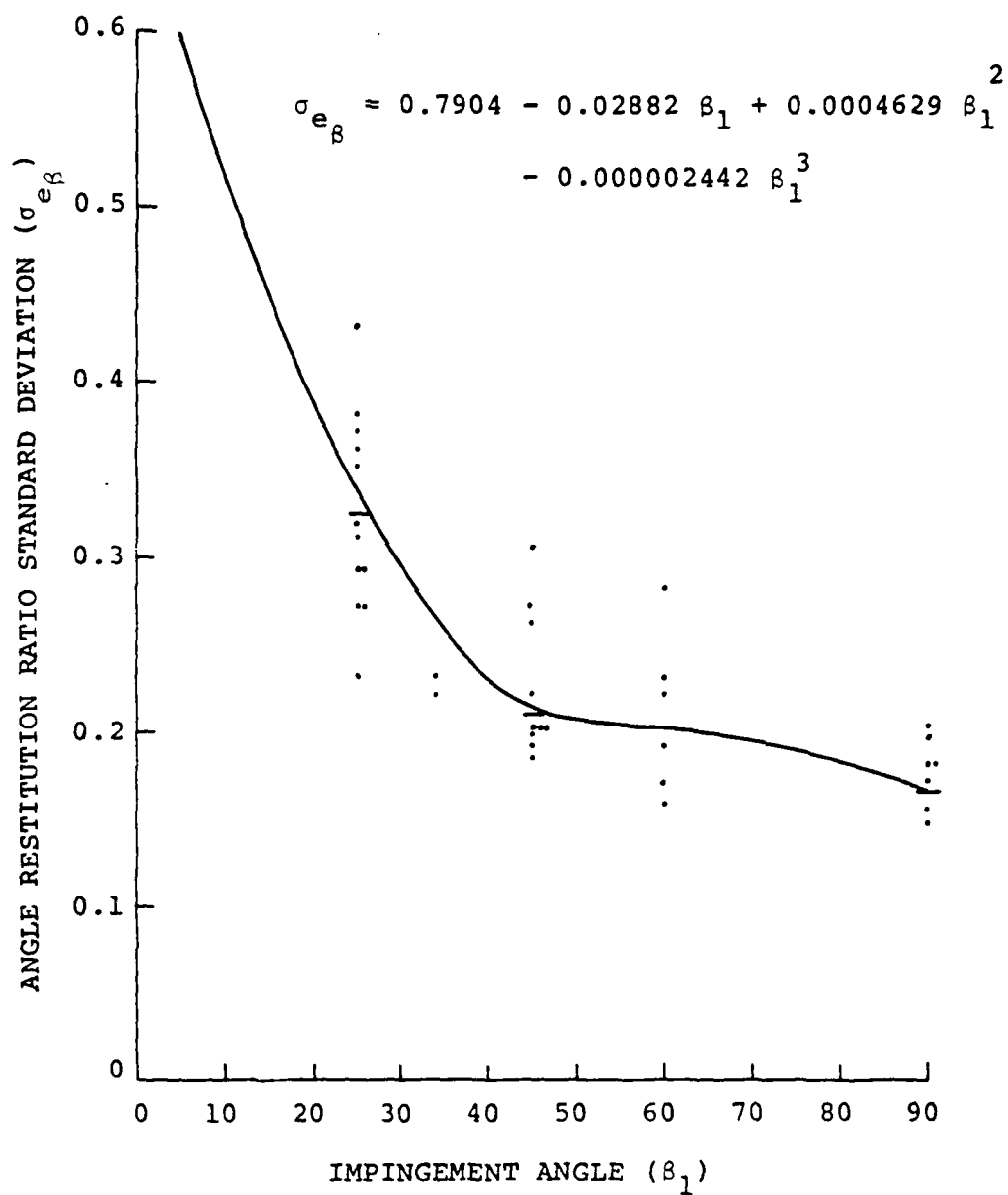
FIG. 14. RELATIONSHIP OF THE ANGLE RESTITUTION RATIO STANDARD DEVIATION WITH IMPINGEMENT ANGLE.

42

$$\sigma_{e_v} = 0.1785 - 0.00178 \, \beta_1 + 0.0000142 \, \beta_1^2$$
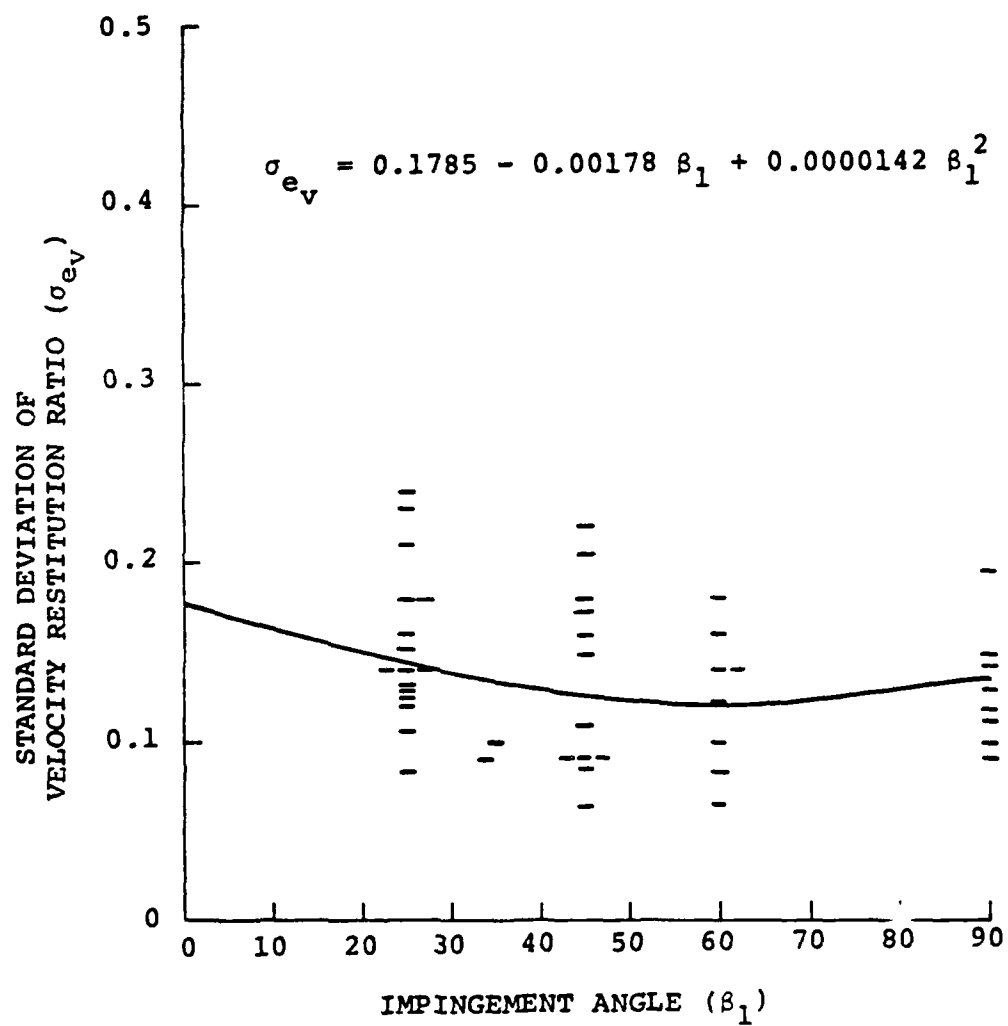
FIG. 15.   RELATIONSHIP OF THE VELOCITY RESTITUTION RATIO
STANDARD DEVIATION WITH IMPINGEMENT ANGLE.

43
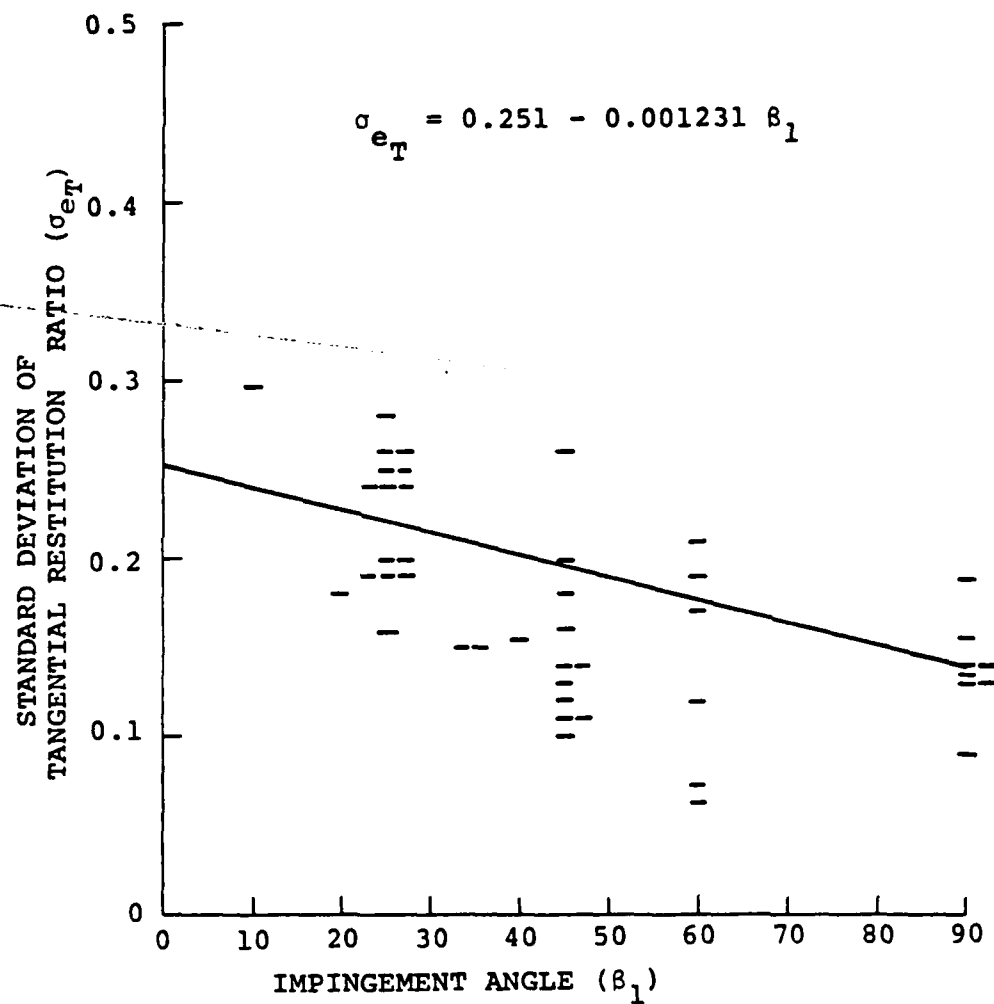
FIG. 16. RELATIONSHIP OF THE TANGENTIAL VELOCITY RESTITUTION RATIO STANDARD DEVIATION WITH IMPINGEMENT ANGLE.

44
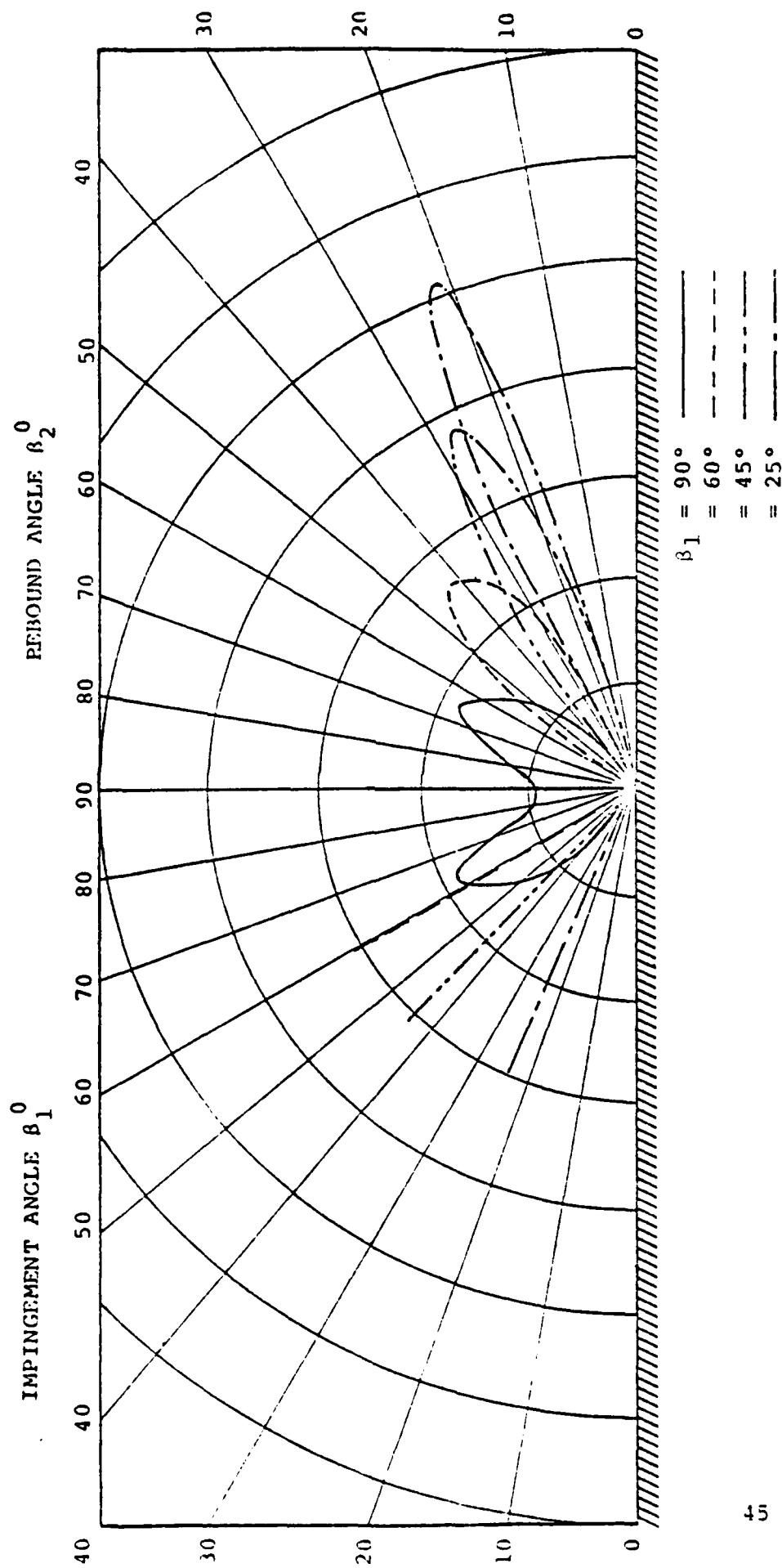
FIG. 17. PARTICLE REBOUND ANGLE DENSITY DISTRIBUTIONS

$\beta_1 = 90°$
$= 60°$
$= 45°$
$= 25°$

REBOUND ANGLE β_2^0

IMPINGEMENT ANGLE β_1^0

45
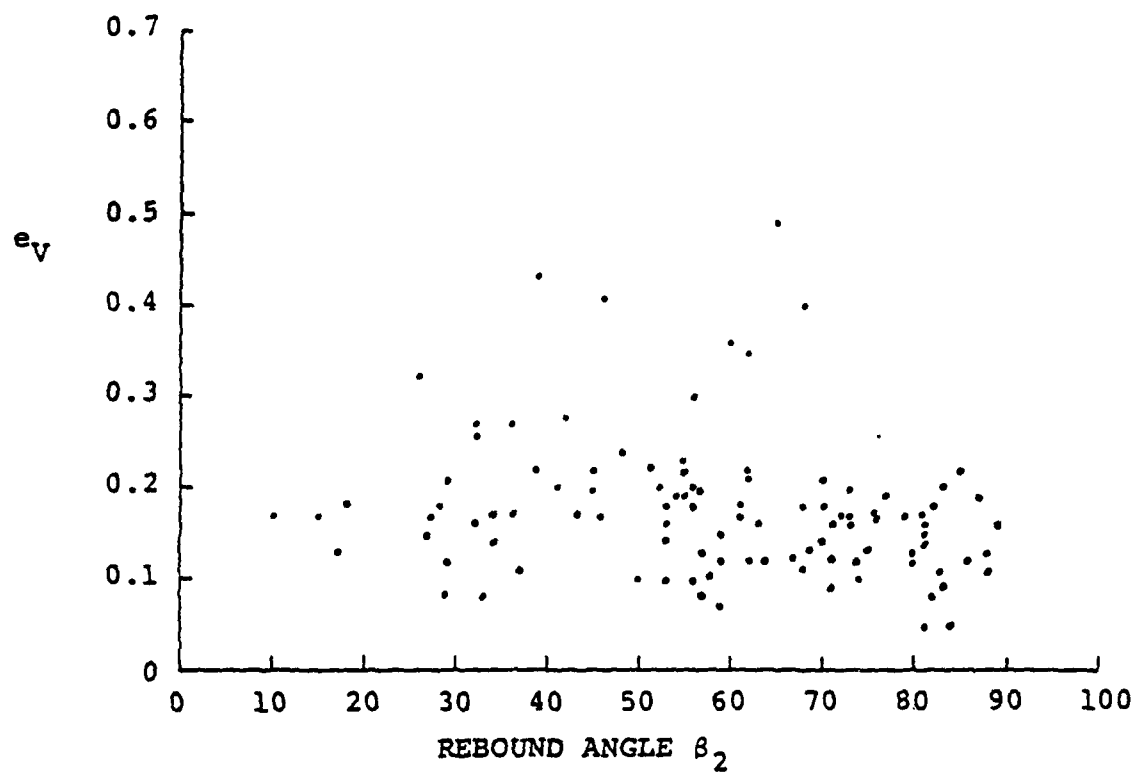
FIG. 18. VELOCITY RESTITUTION RATIO VERSUS REBOUNDING
ANGLE β_2.
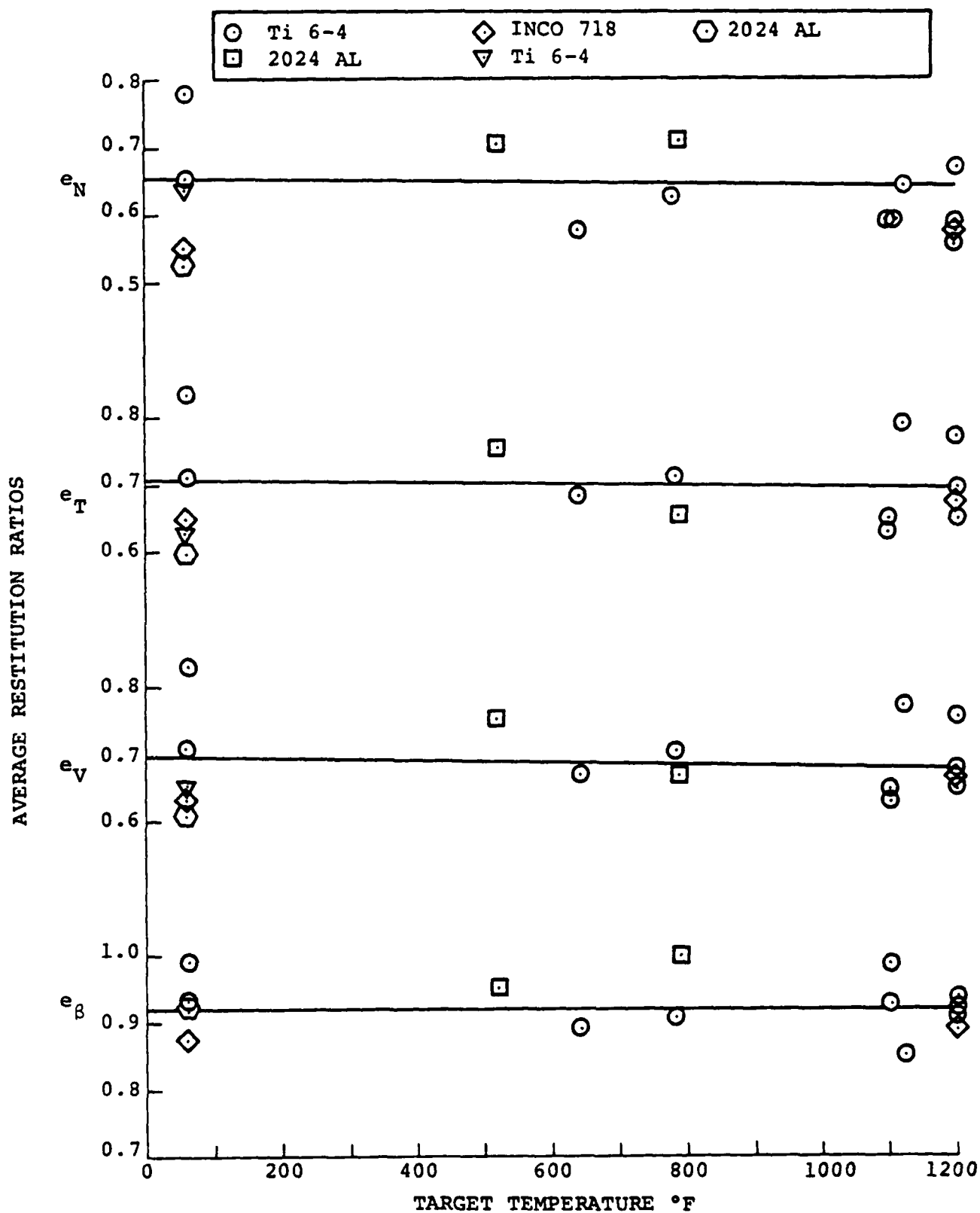
FIG. 19. AVERAGE RESTITUTION RATIOS VERSUS TARGET TEMPERATURE FOR A
25° IMPINGEMENT ANGLE.
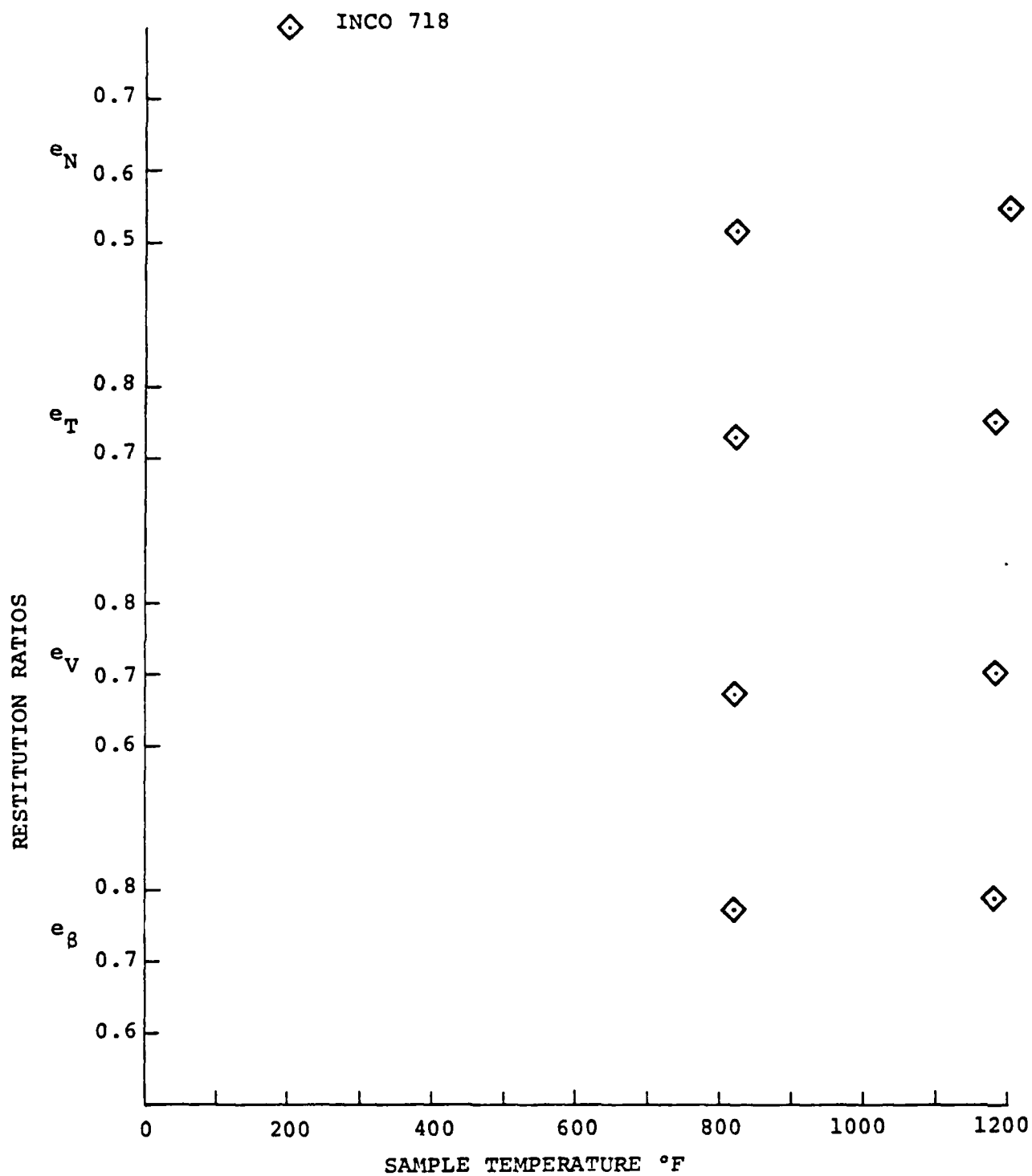
FIG. 20. IMPORTANT RESTITUTION RATIOS (AVE.) VS. SAMPLE
TEMPERATURE @ $\beta_1 = 35°$.

48
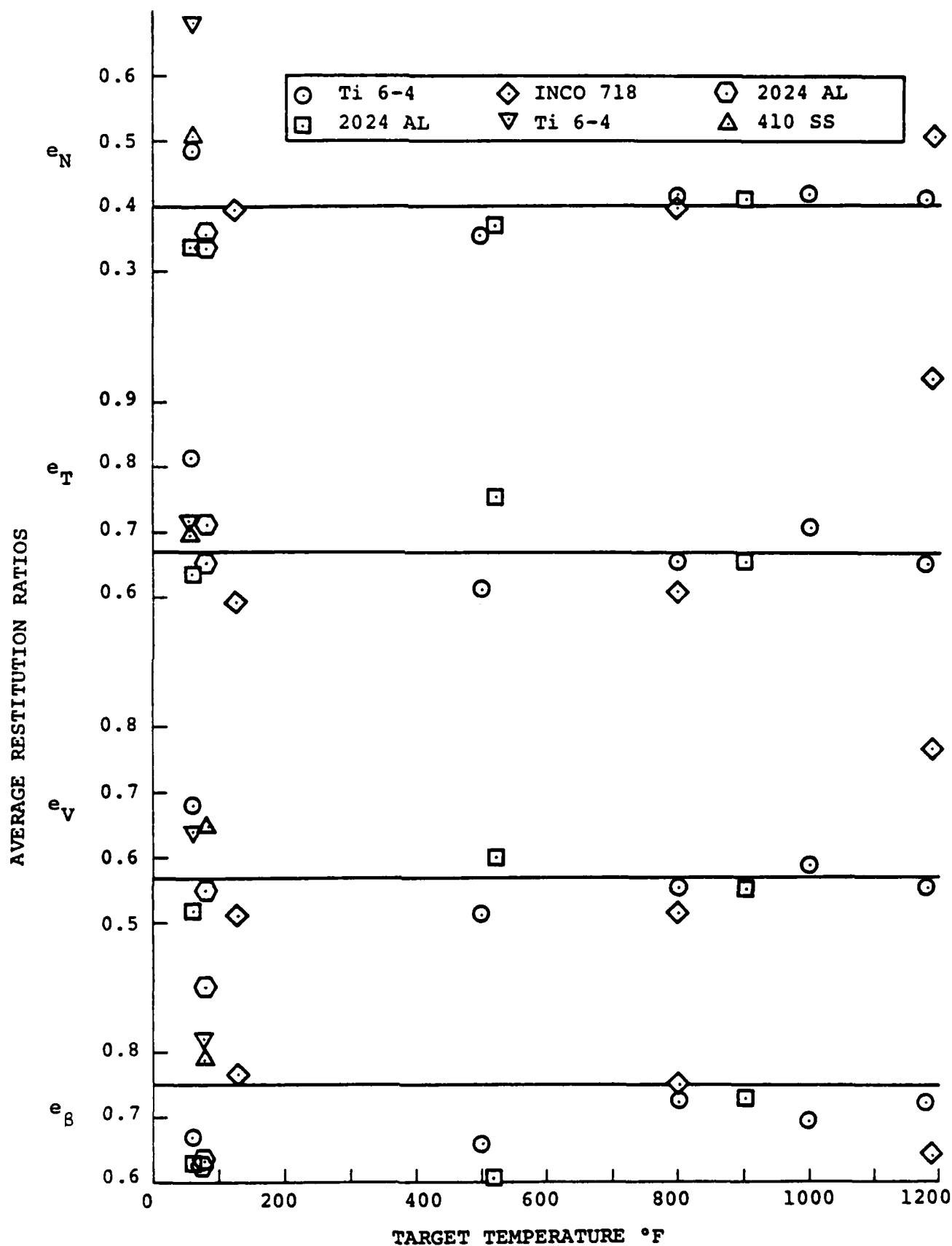
FIG. 21.   AVERAGE RESTITUTION RATIOS VS. TARGET TEMPERATURE FOR A
45° IMPINGEMENT ANGLE.

49
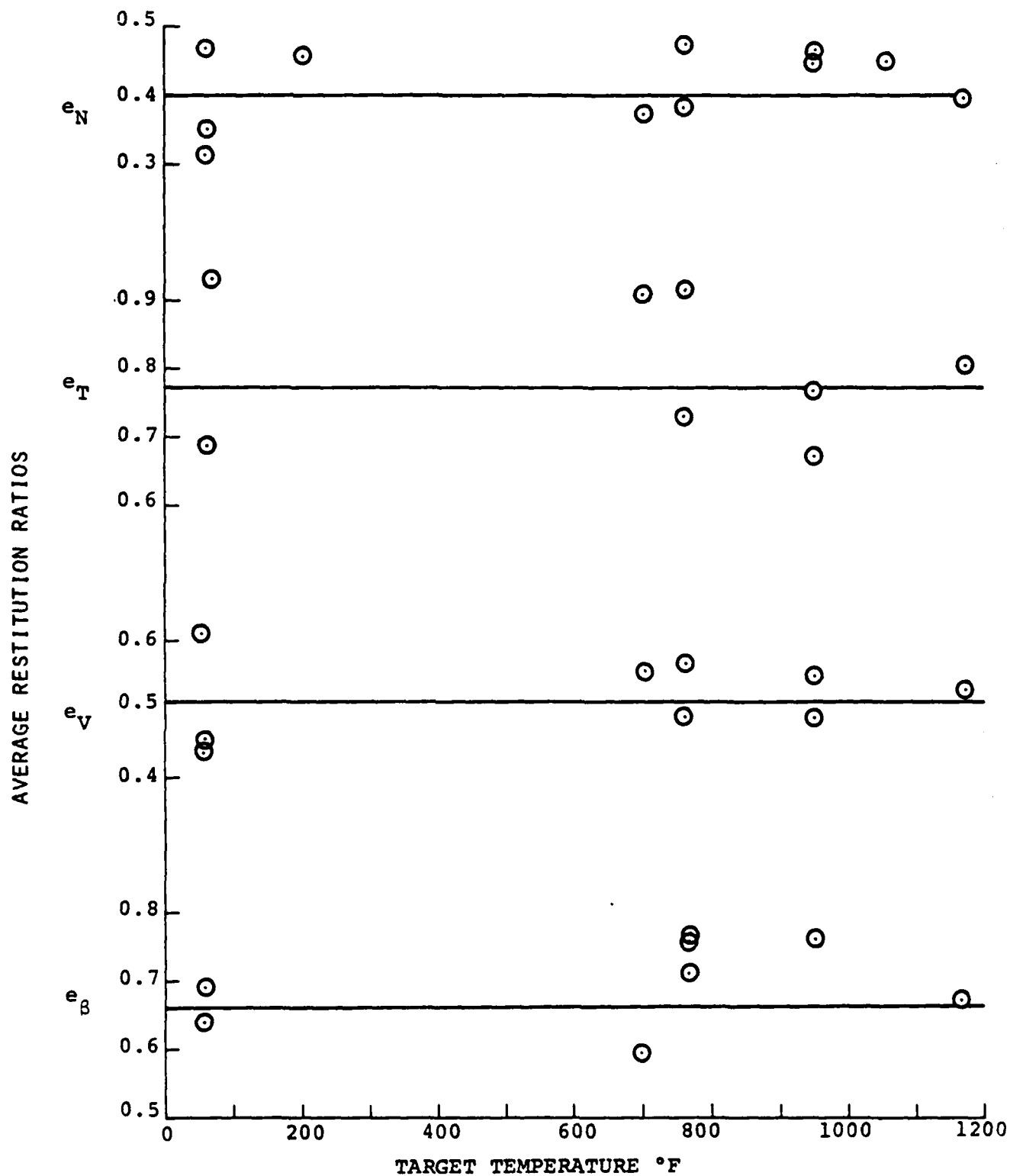
FIG. 22. . AVERAGE RESTITUTION RATIOS VERSUS TARGET TEMPERATURE FOR A 60° IMPINGEMENT ANGLE AND Ti 6-4 TARGET MATERIAL.

50
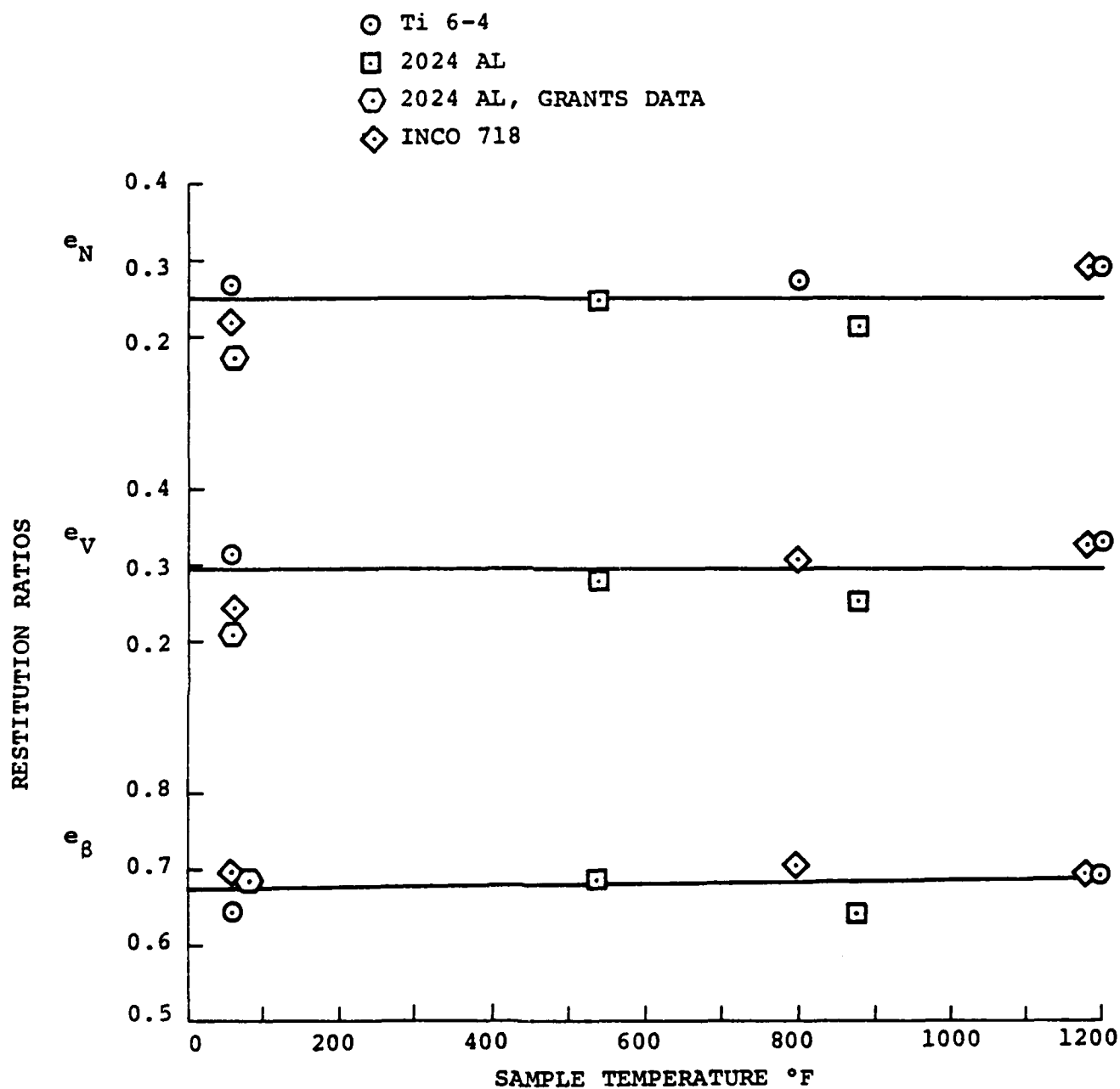
FIG. 23. IMPORTANT RESTITUTION RATIOS (AVE.) VS. SAMPLE TEMPERATURE @ $\beta_1 = 90°$.
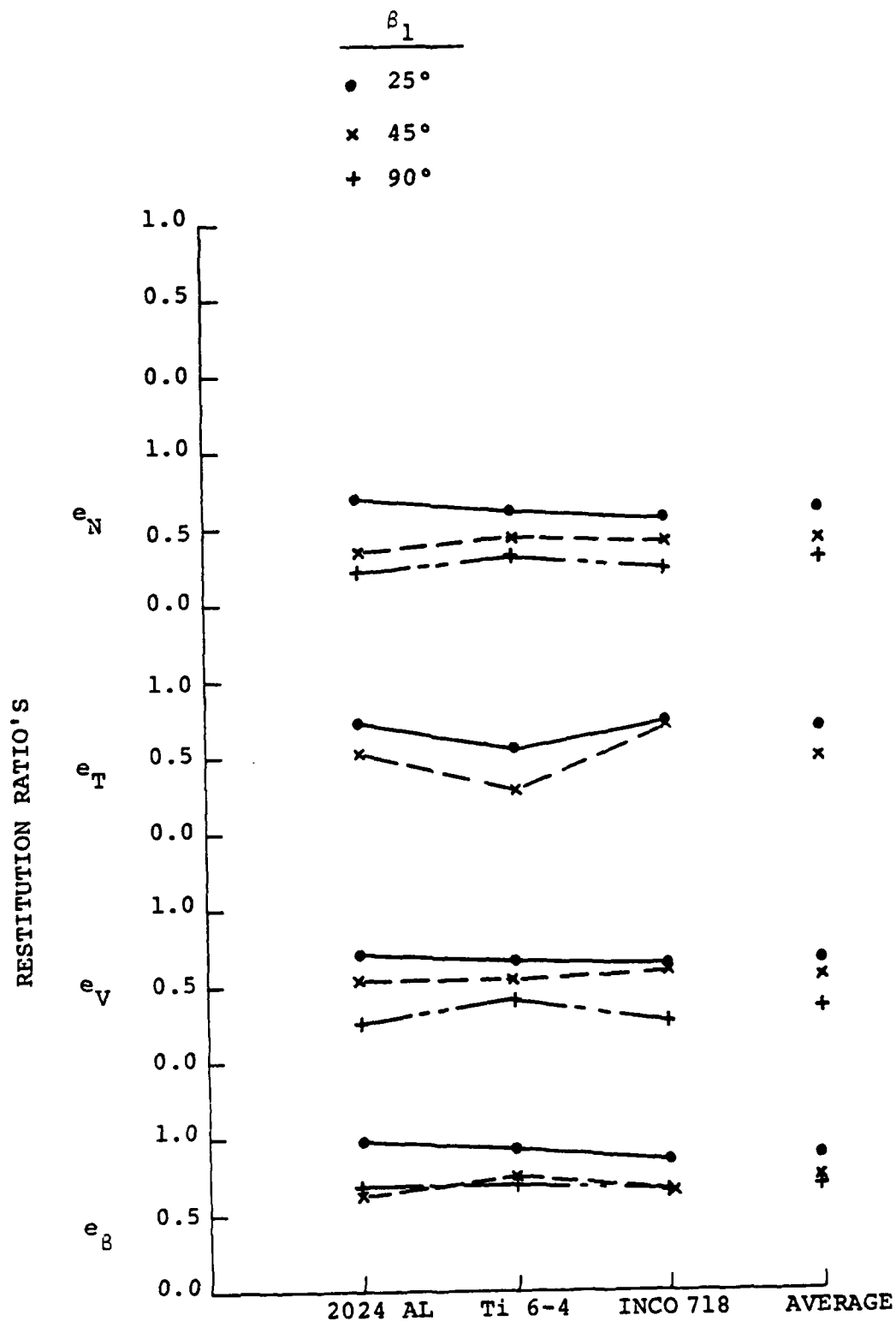
FIG. 24 . COMPARISON OF PARTICLE RESTITUTION RATIO AMONG
TARGET MATERIALS.

52
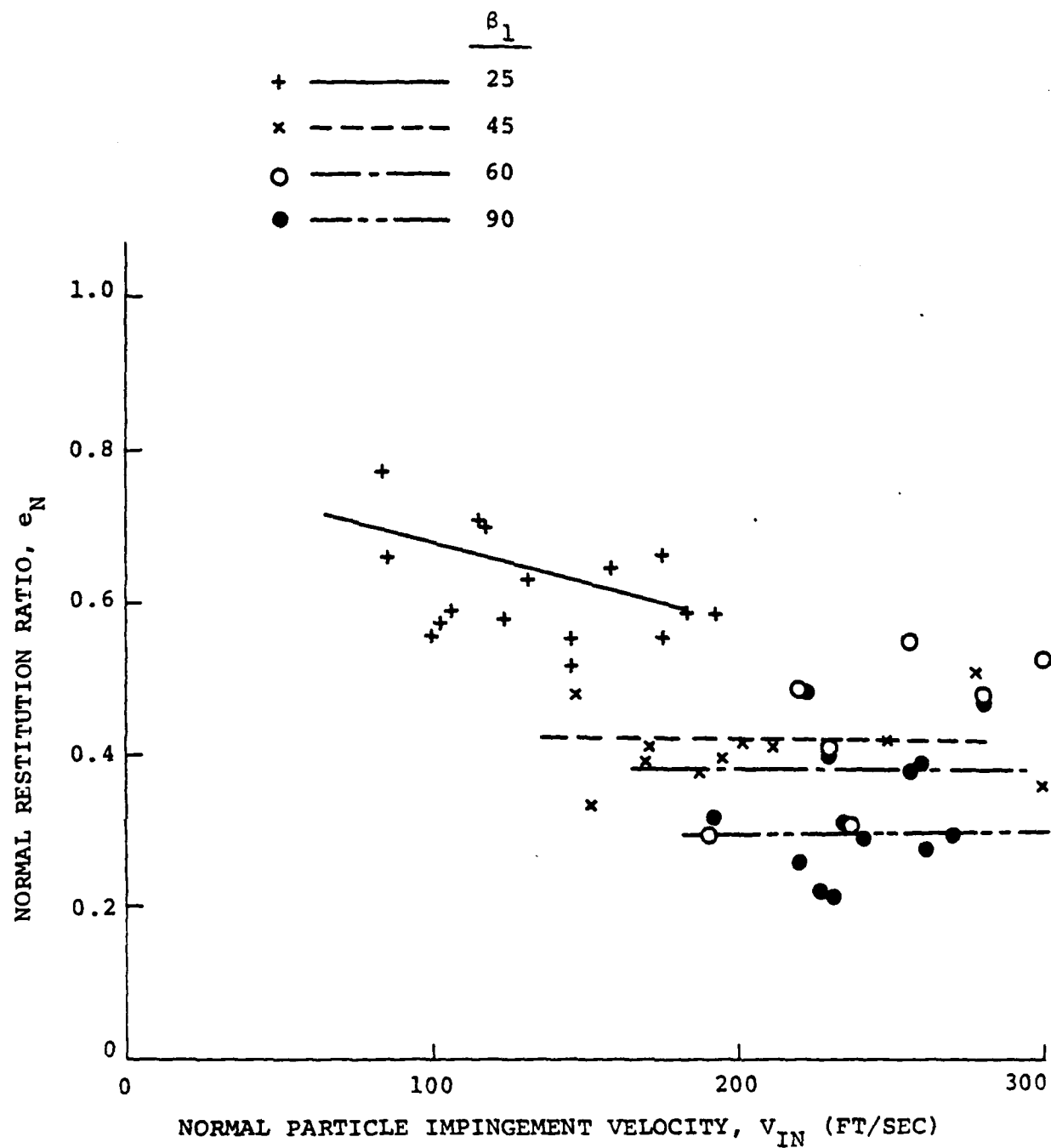
FIG. 25 . NORMAL RESTITUTION RATIO RELATIVE TO NORMAL PARTICLE IMPINGEMEN
VELOCITY FOR CONSTANT IMPINGEMENT ANGLE - APPLIES FOR
INCO 718, Ti 6-4 & 2024 AL TARGET MATERIAL.

53

FIG. 26. TANGENTIAL RESTITUTION RATIO RELATIVE TO TANGENTIAL PARTICLE
IMPINGEMENT VELOCITY FOR CONSTANT IMPINGEMENT ANGLE -
APPLIES FOR INCO 718, Ti 6-4 & 2024 AL TARGET MATERIAL.

54

$$e_\beta = 1.0 - 2.23 \, E - 4\beta_1^2 + 2.08 \, E - 6\beta_1^3$$

ABSOLUTE AVERAGE

STANDARD DEVIATION

$$\sigma_{e_\beta} = 0.7905 - 0.02882 \, \beta_1$$
$$+ 4.629 \, E - 4 \, \beta_1^2 - 2.442E - 6\beta_1^3$$
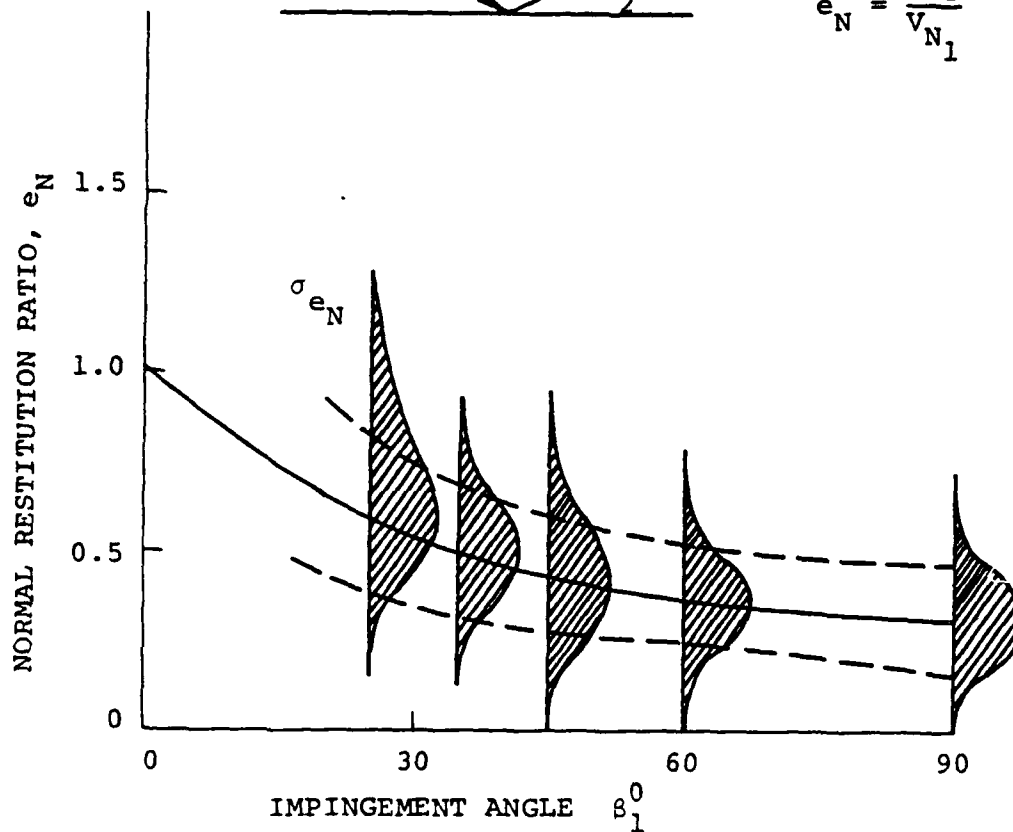
AVERAGE

$$e_\beta = \frac{\beta_2}{\beta_1}$$
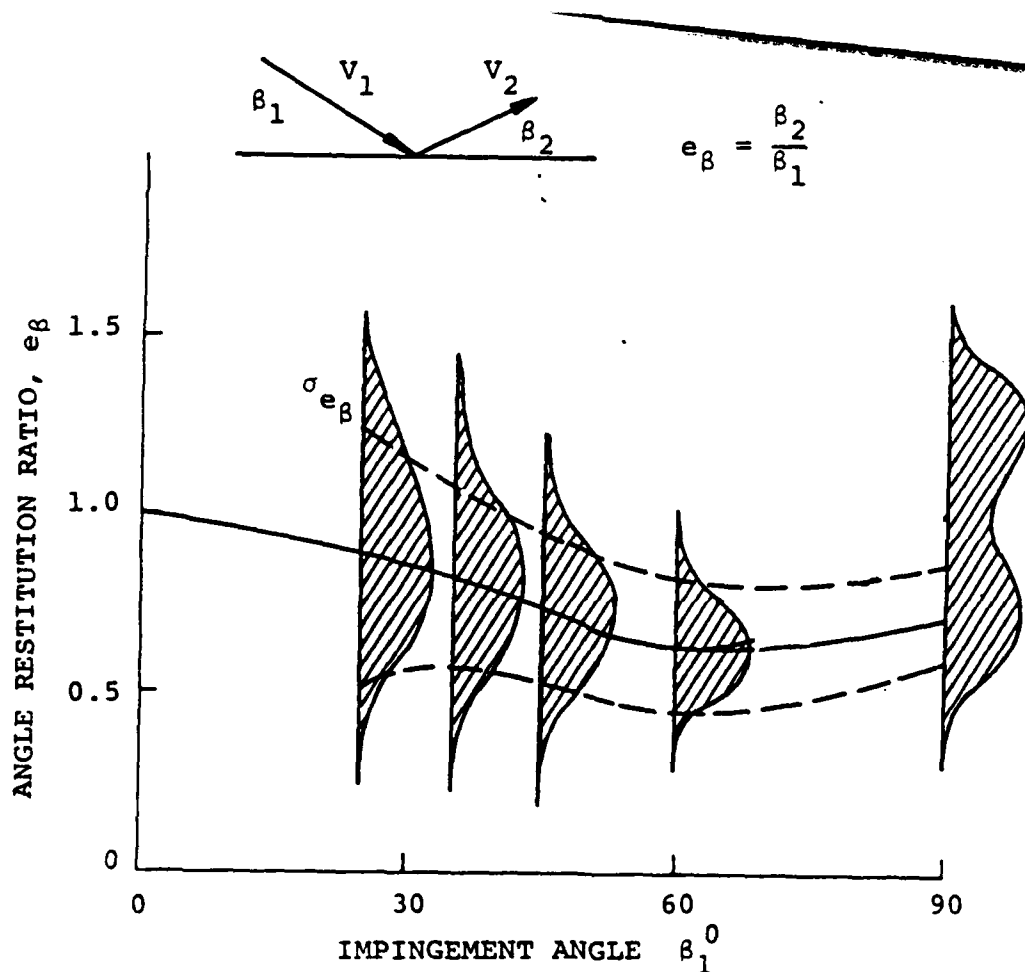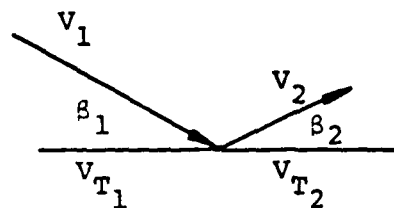
FIG. 27. INFLUENCE OF IMPINGEMENT ANGLE ON PARTICLE REBOUND ANGLE RESTITUTION RATIO FOR INCO 718, Ti 6-4 & 2024 AL TARGET MATERIAL.

55

$$e_v = 1.0 - 0.179\,\beta_1 + 2.56\;E-4\;\beta_1^2 - 1.52\;E-6\;\beta_1$$

$$\sigma_{e_v} = 0.1785 - 1.78\;E-3\;\beta_1 + 1.42E-5\;\beta_1^2$$

$$e_v = \frac{V_2}{V_1}$$
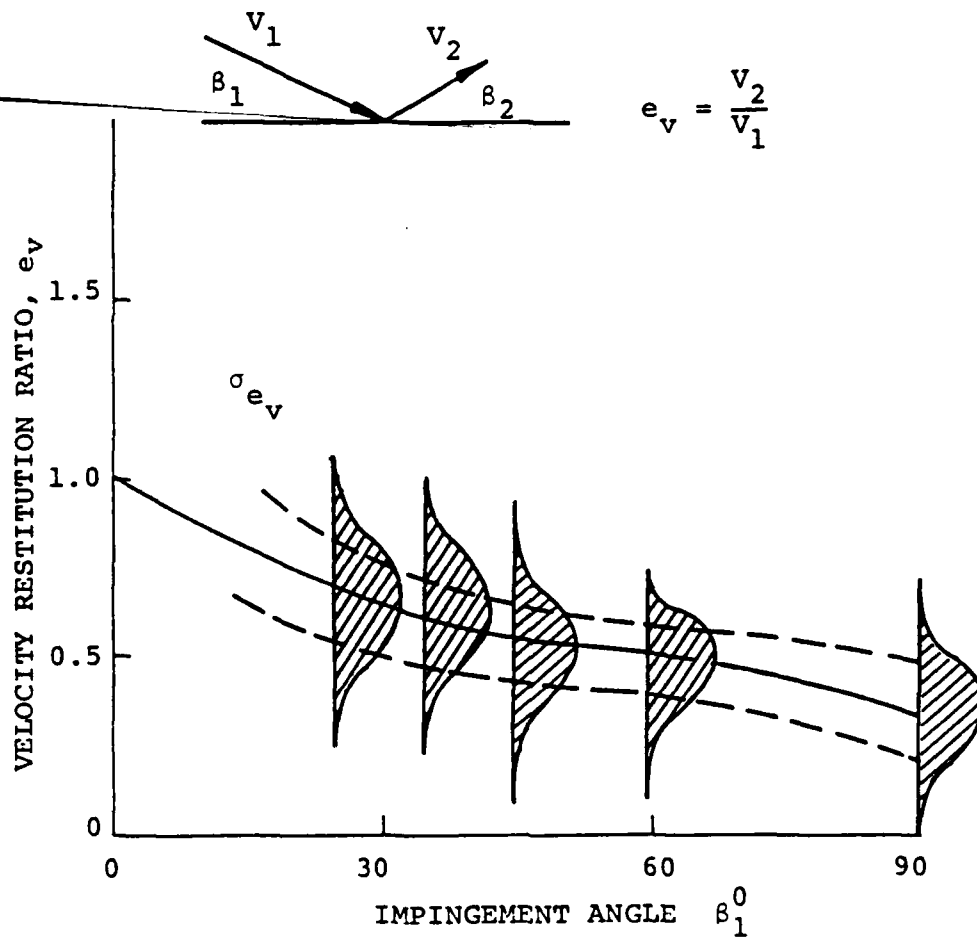
FIG. 28. INFLUENCE OF IMPINGEMENT ANGLE ON PARTICLE REBOUND VELOCITY
RESTITUTION RATIO FOR INCO 718, Ti 6-4 & 2024 AL
TARGET MATERIALS.

$$e_N = 1.0 - 0.0211 + 2.28\ E - 4\ \beta_1^2 - 8.76\ E - 7\ \beta_1^3$$

$$\sigma_{e_N} = 0.362 - 6.85\ E - 3\ \beta_1 + 4.87\ E - 5\ \beta_1^3$$
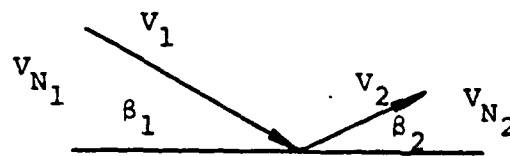
$$e_N = \frac{V_{N_2}}{V_{N_1}}$$

FIG. 29.   INFLUENCE OF IMPINGEMENT ANGLE ON PARTICLE NORMAL VELOCITY
RESTITUTION RATIO FOR INCO 718, Ti 6-4 & 2024 AL
TARGET MATERIALS.

57

$$e_T = 0.953 - 4.46 \beta_1^2 + 6.48\ E - 6\ \beta_1^3$$

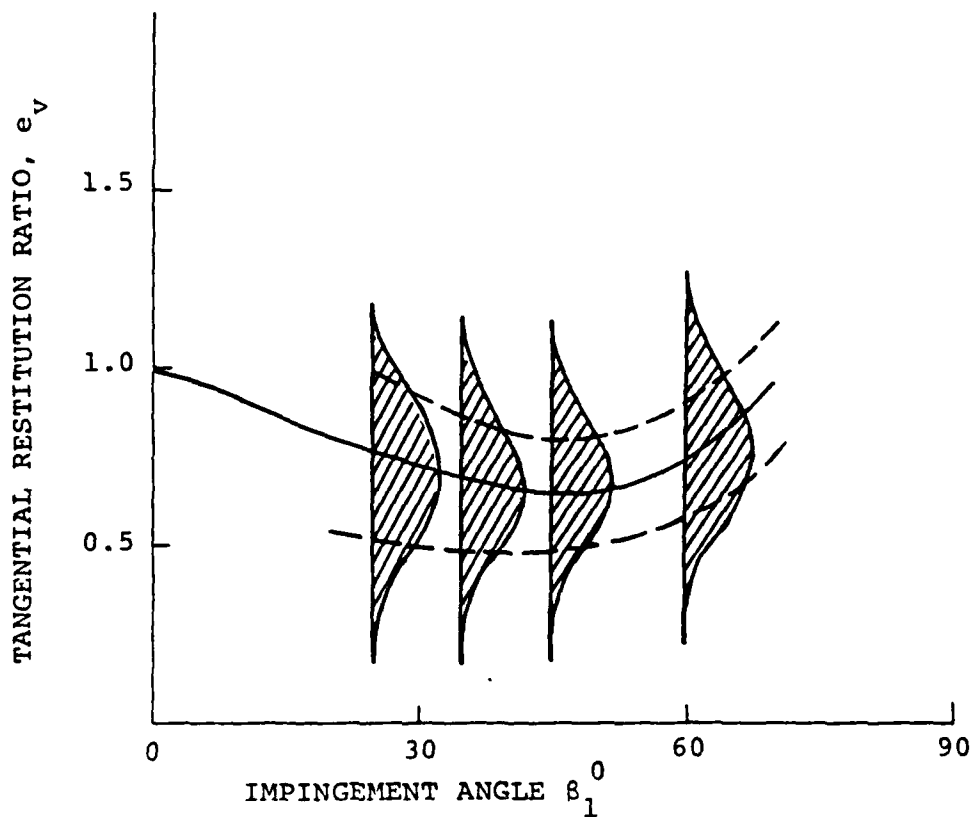$$\sigma_{e_T} = 0.251 - 0.00123\ \beta_1$$

$$e_v = \frac{V_{T_2}}{V_{T_1}}$$

FIG. 30. INFLUENCE OF IMPINGEMENT ANGLE ON PARTICLE TANGENTIAL
VELOCITY RESTITUTION RATIO FOR INCO 718, Ti 6-4 & 2024 AL
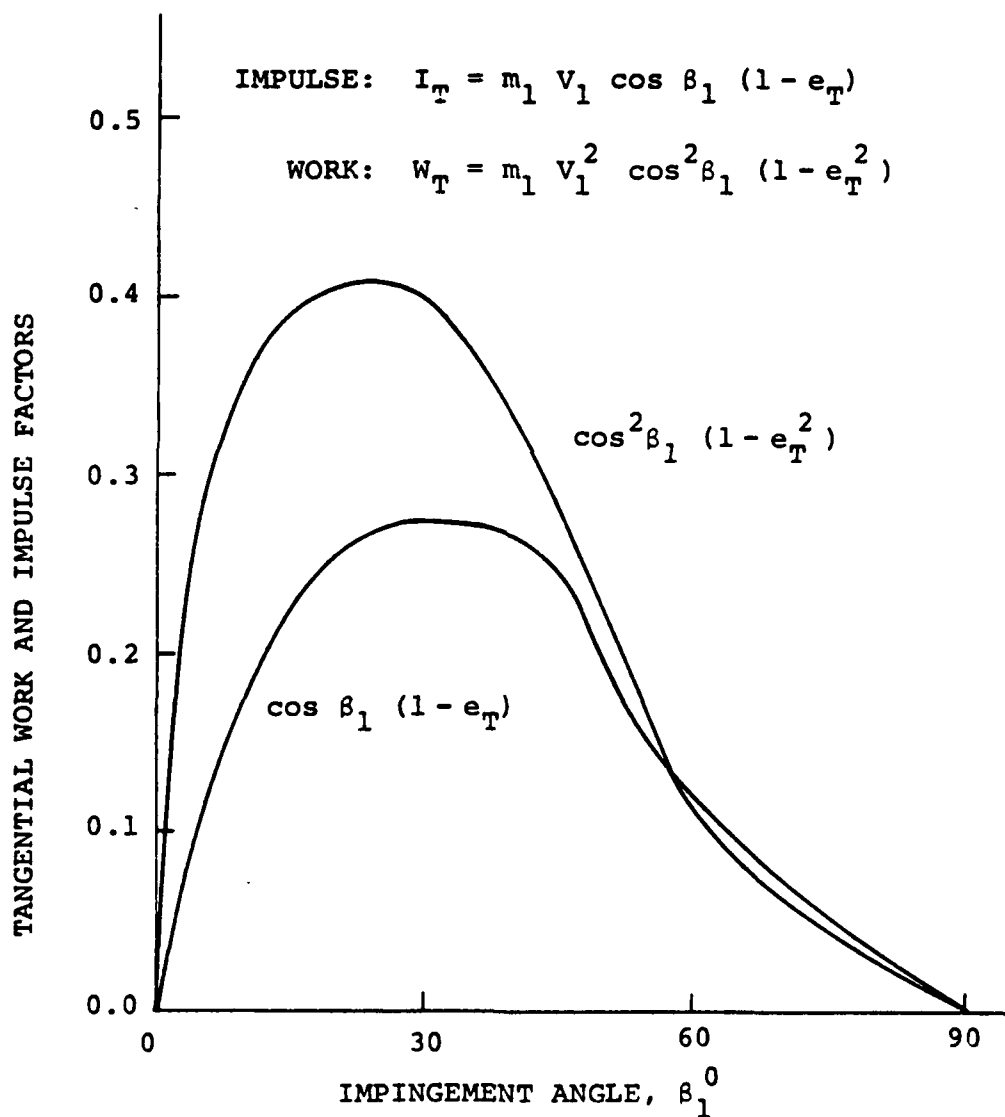TARGET MATERIAL.

IMPULSE: $I_T = m_1 V_1 \cos \beta_1 (1 - e_T)$

WORK: $W_T = m_1 V_1^2 \cos^2 \beta_1 (1 - e_T^2)$

$\cos^2 \beta_1 (1 - e_T^2)$

$\cos \beta_1 (1 - e_T)$

TANGENTIAL WORK AND IMPULSE FACTORS

IMPINGEMENT ANGLE, β_1^0

FIG. 31. WORK AND IMPULSE IN TANGENTIAL DIRECTION RELATIVE TO IMPINGEMENT ANGLE - APPLIES FOR INCO 718, Ti 6-4 & 2024 AL TARGET MATERIAL.

59
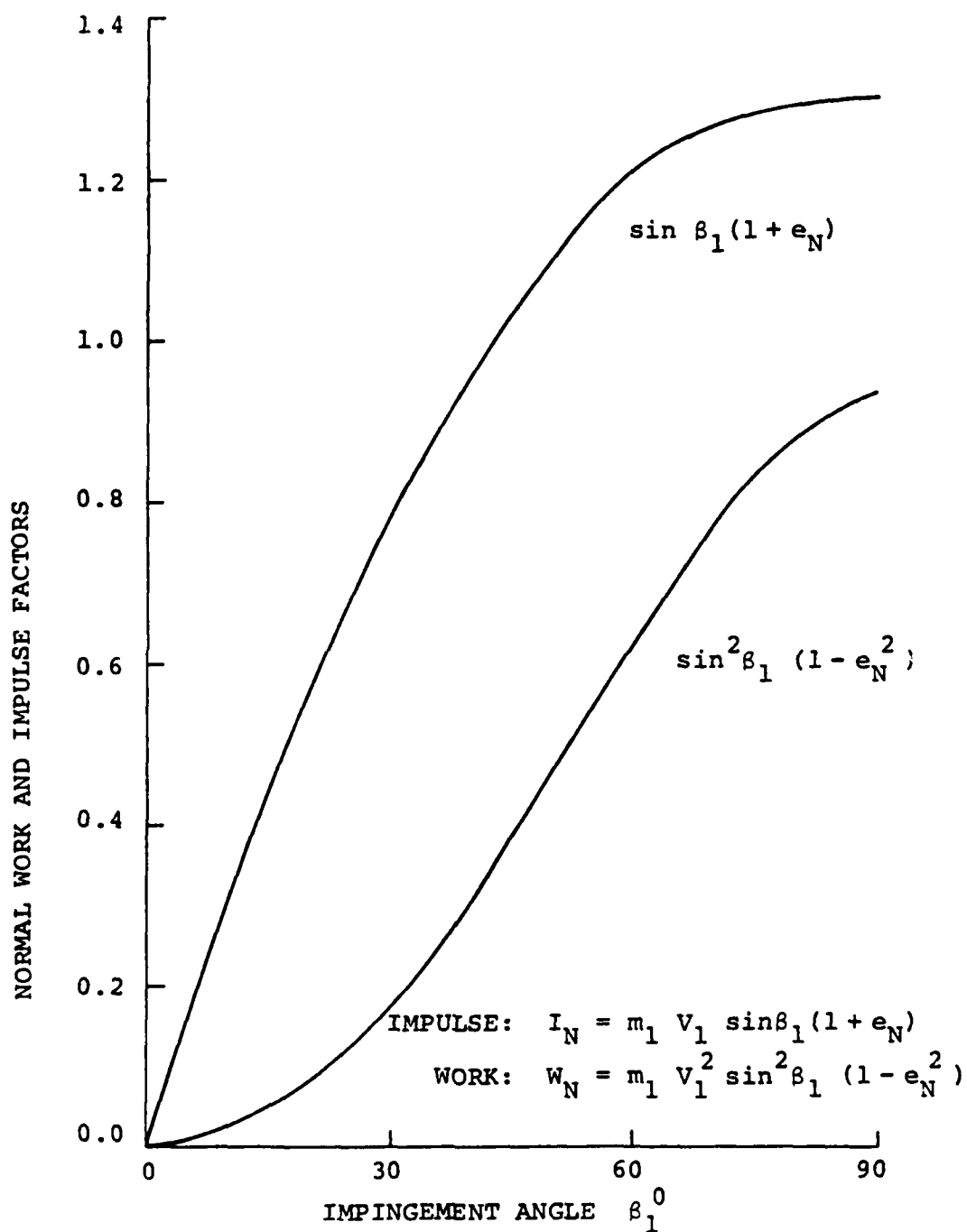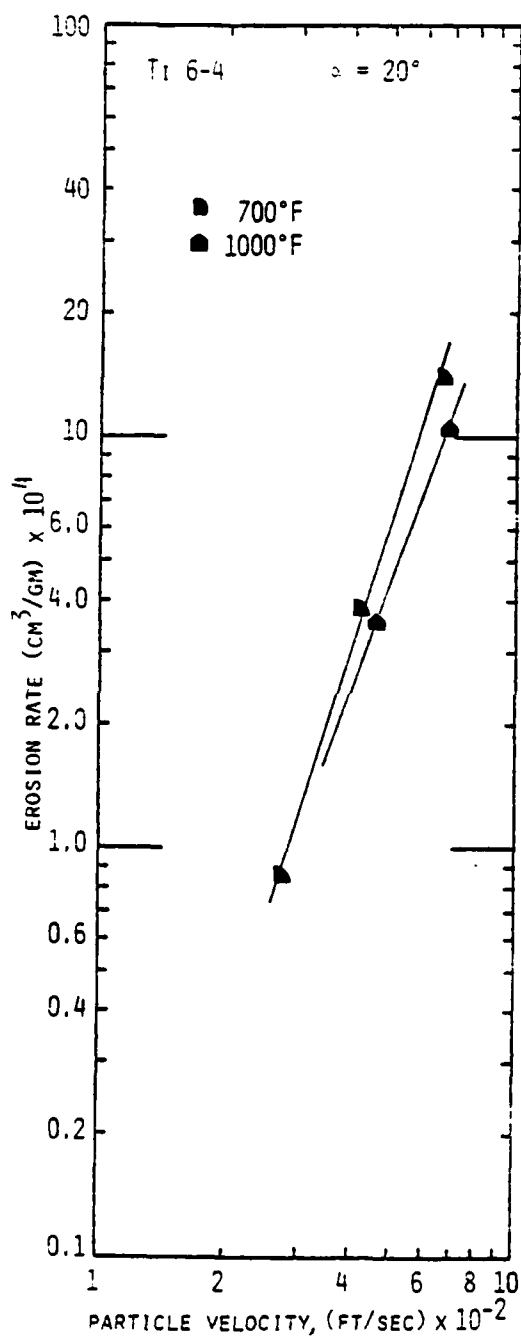
FIG. 32 . WORK AND IMPULSE IN NORMAL DIRECTION RELATIVE TO
IMPINGEMENT ANGLE — APPLIES FOR INCO 718, Ti 6-4 &
INCO 718 TARGET MATERIAL.

60

FIG. 33. Ti 6-4 EROSION RATE VERSUS   FIG. 34.   Ti 6-4 EROSION RATE VERSUS
         PARTICLE VELOCITY FOR   PARTICLE VELOCITY FOR
         DIFFERENT SAMPLE TEMPERATURES,   DIFFERENT SAMPLE TEMPERA-
         α = 20°.   TURES, α = 25°.
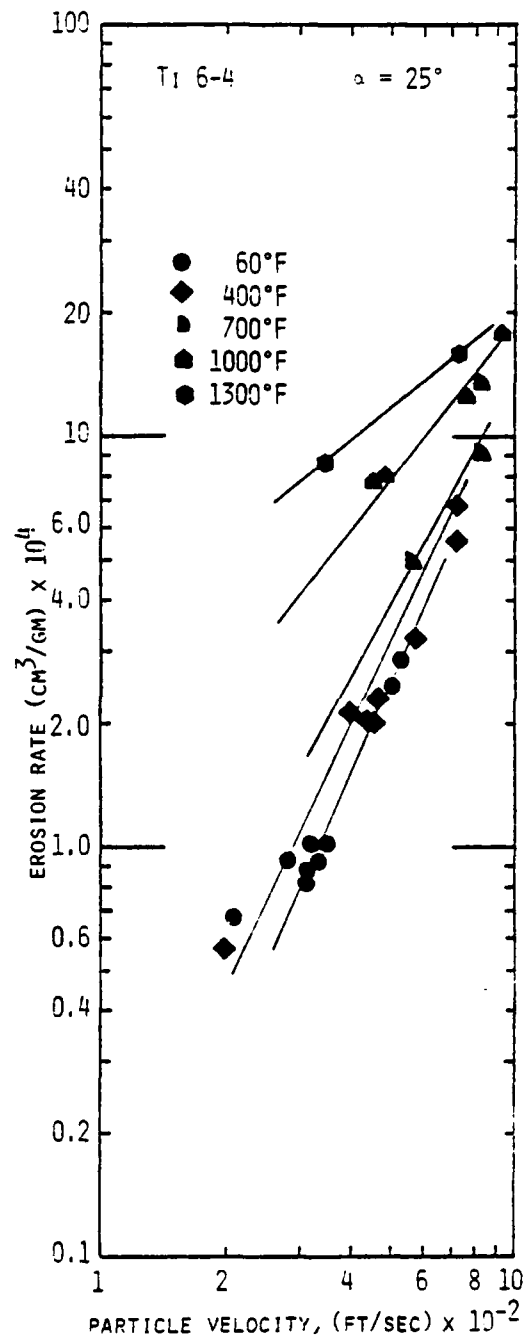
61
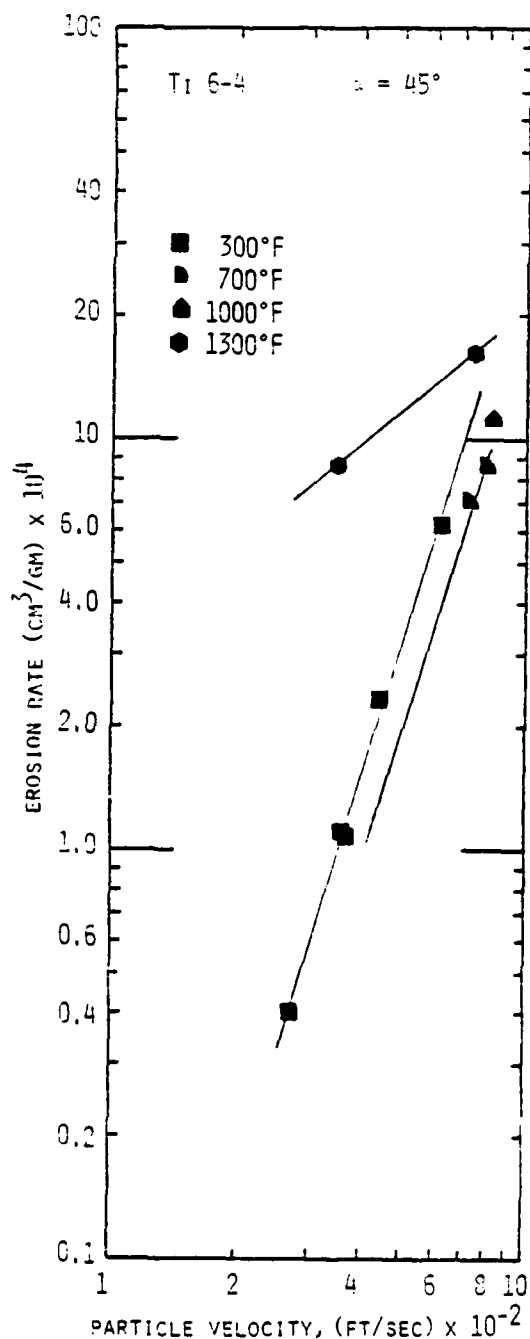
FIG. 35. Ti 6-4 EROSION RATE VERSUS   FIG. 36. Ti 6-4 EROSION RATE VERSUS
          PARTICLE VELOCITY FOR   PARTICLE VELOCITY FOR
          DIFFERENT SAMPLE TEMPERATURES,   DIFFERENT SAMPLE TEMPERATURES,
          α = 45°.   α = 90°.
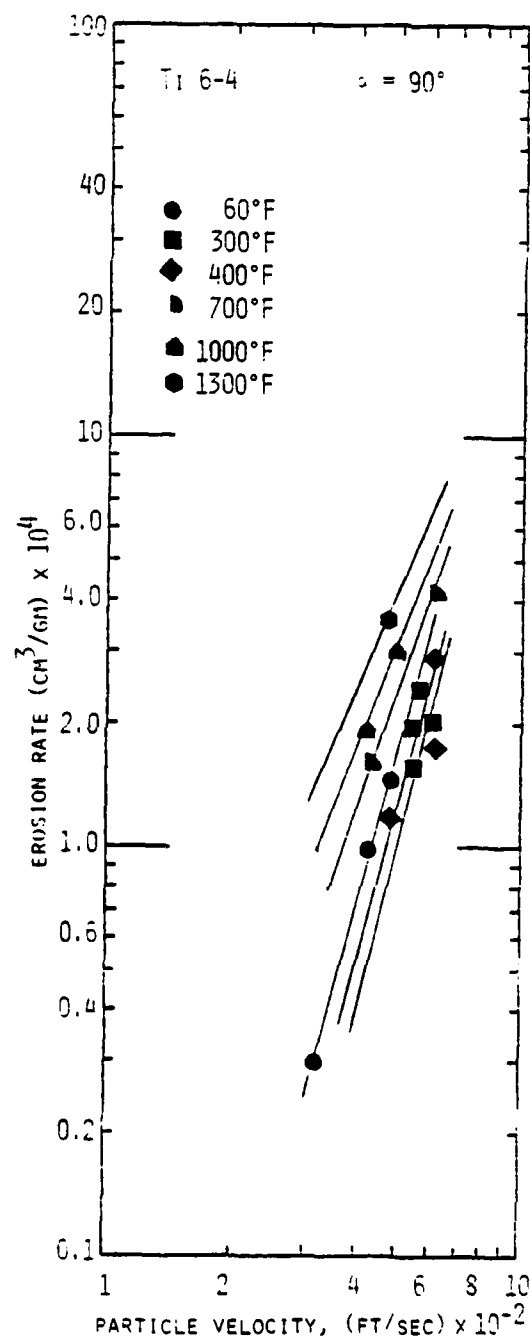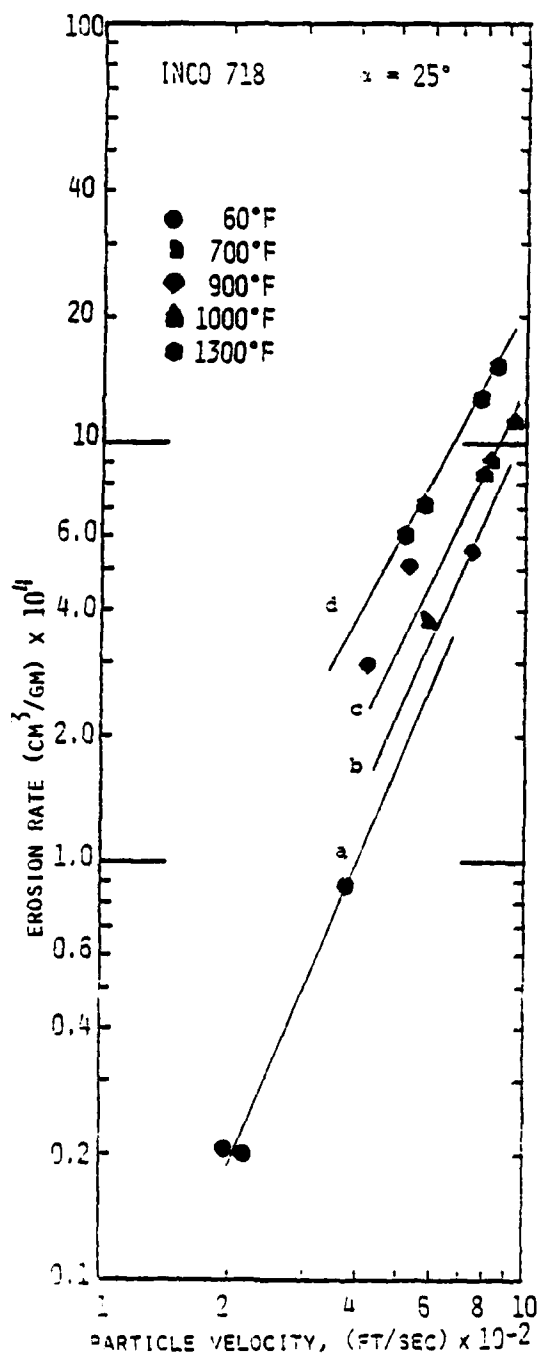
FIG. 37.   INCO 718 EROSION RATE VERSUS   FIG. 38.   INCO 718 EROSION RATE VERSUS
PARTICLE VELOCITY FOR   PARTICLE VELOCITY FOR
DIFFERENT SAMPLE TEMPERATURES,   DIFFERENT SAMPLE TEMPERA-
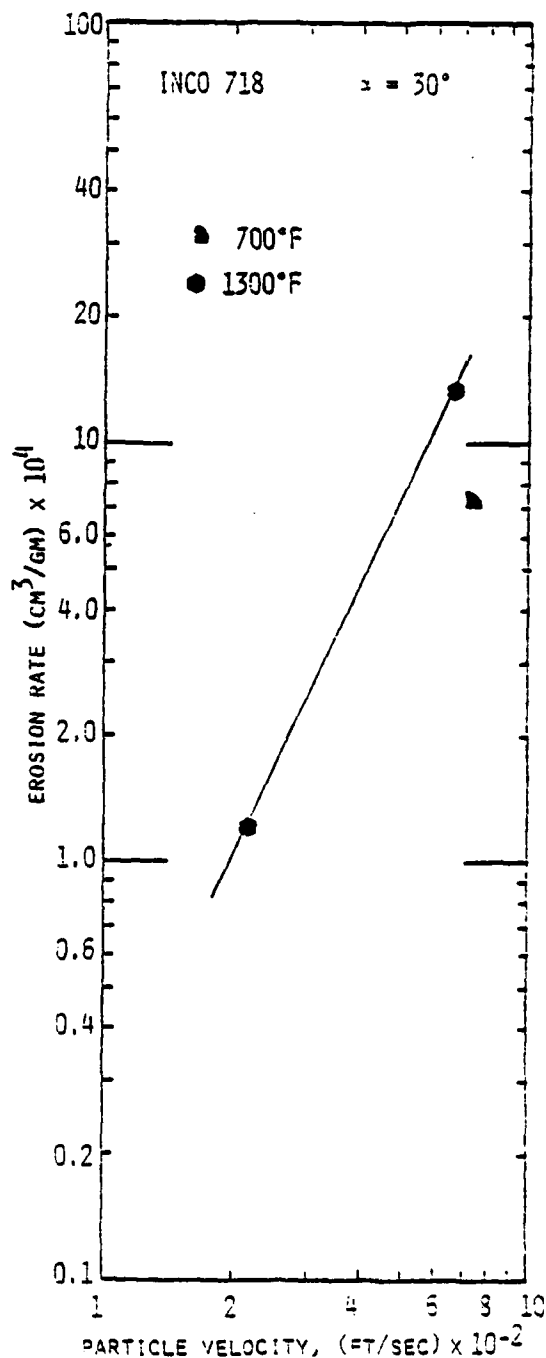α = 25°.   TURES, α = 30°.

63
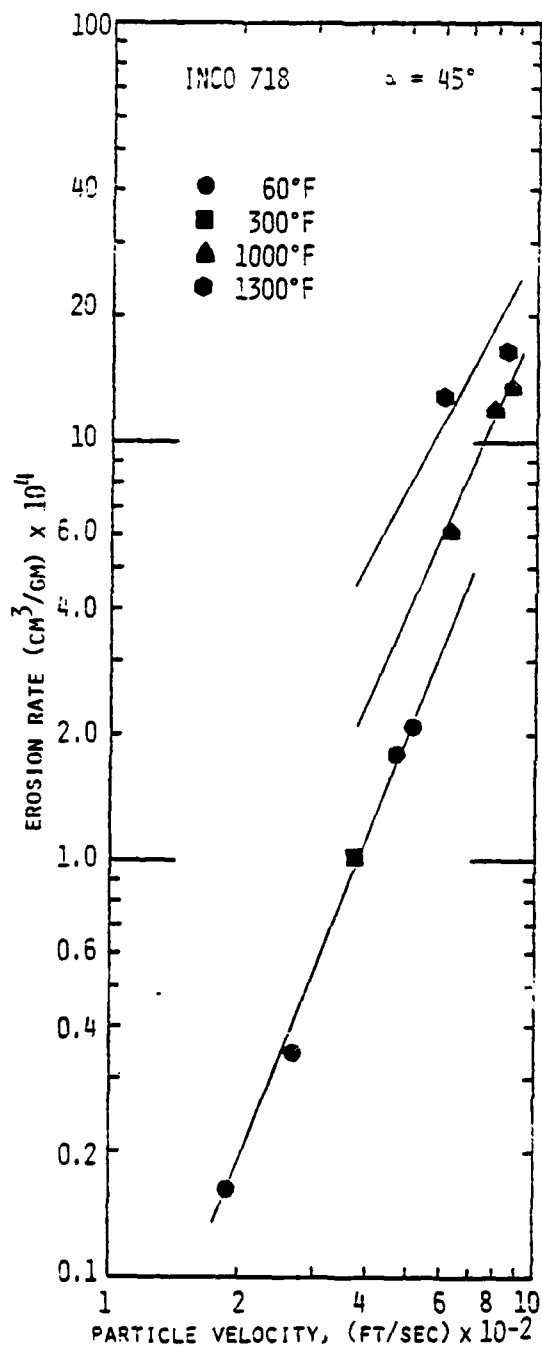
FIG. 39. INCO 718 EROSION RATE VERSUS PARTICLE VELOCITY FOR DIFFERENT SAMPLE TEMPERATURES, α = 45°.
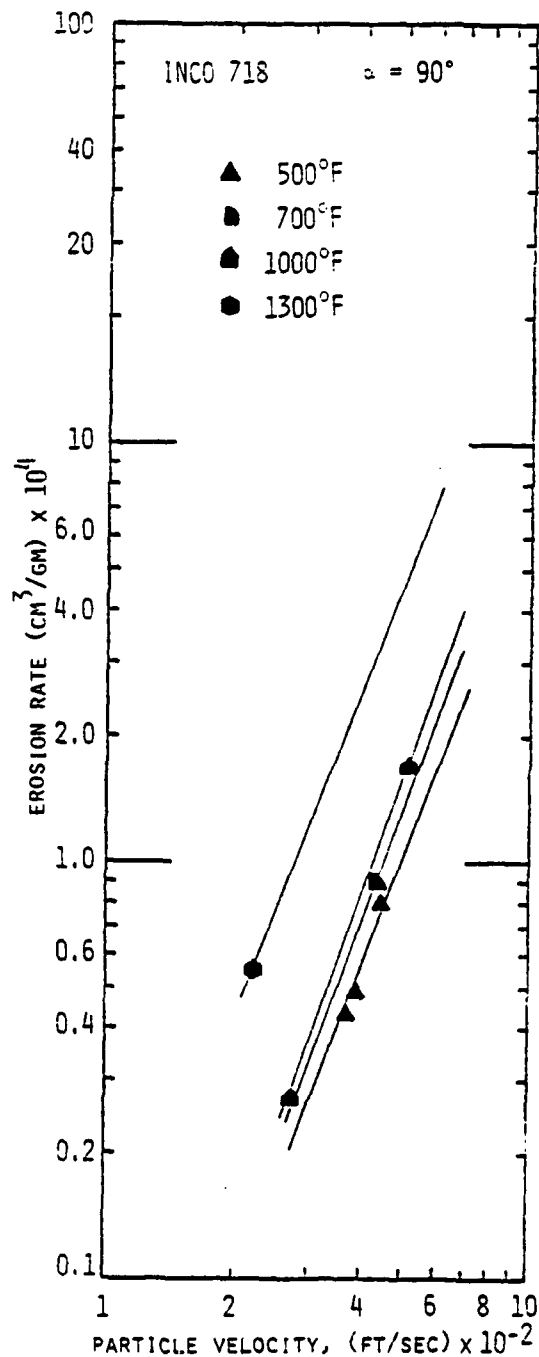
FIG. 40. INCO 718 EROSION RATE VERSUS PARTICLE VELOCITY FOR DIFFERENT SAMPLE TEMPERATURES, α = 90°.

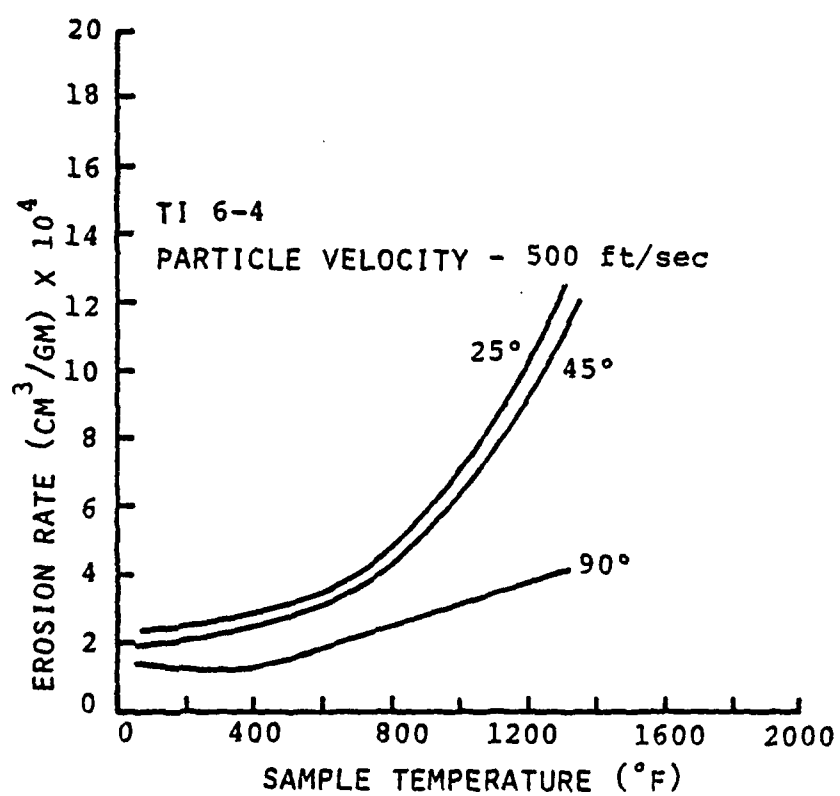FIG. 41.   EROSION RATE VERSUS SAMPLE TEMPERATURE
FOR Ti 6-4, α = 25°, 45° AND 90°.

65

INCO 718
PARTICLE VELOCITY - 500 FT/SEC
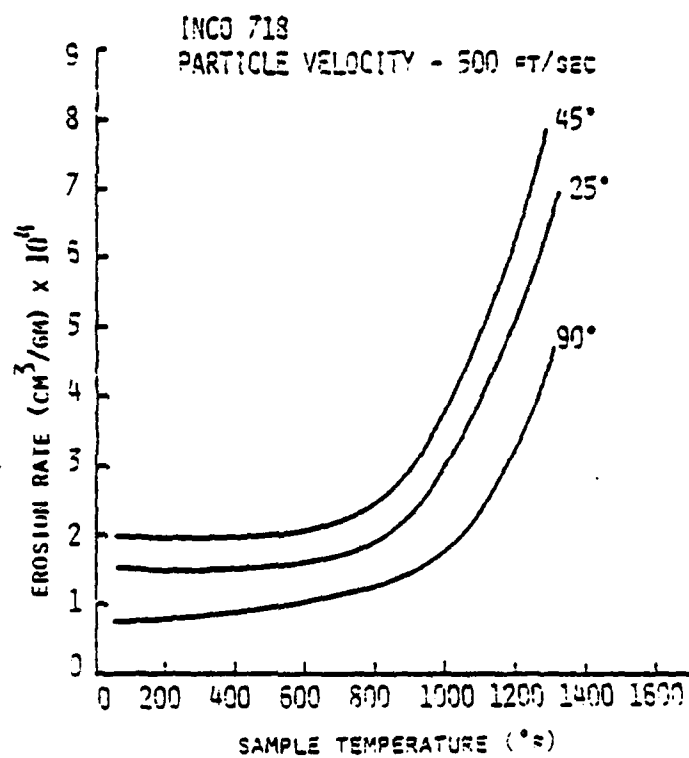
FIG. 42. EROSION RATE VERSUS SAMPLE TEMPERATURE
FOR INCO 718, $\alpha = 25°$, 45° AND 90°.
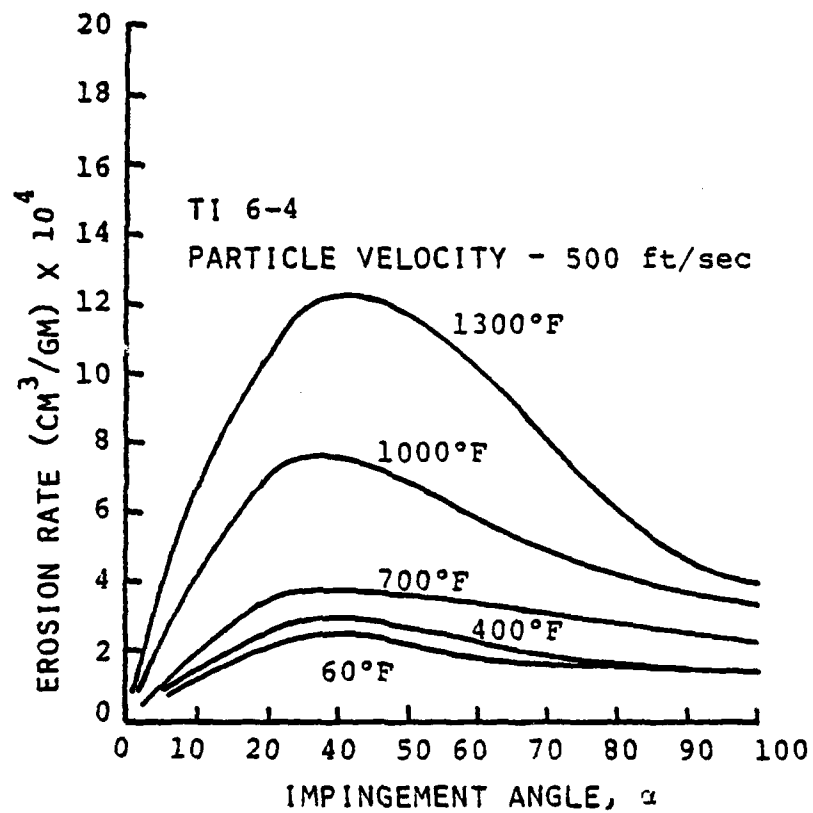
66

FIG. 43.   Ti 6-4 EROSION RATE VERSUS PARTICLE
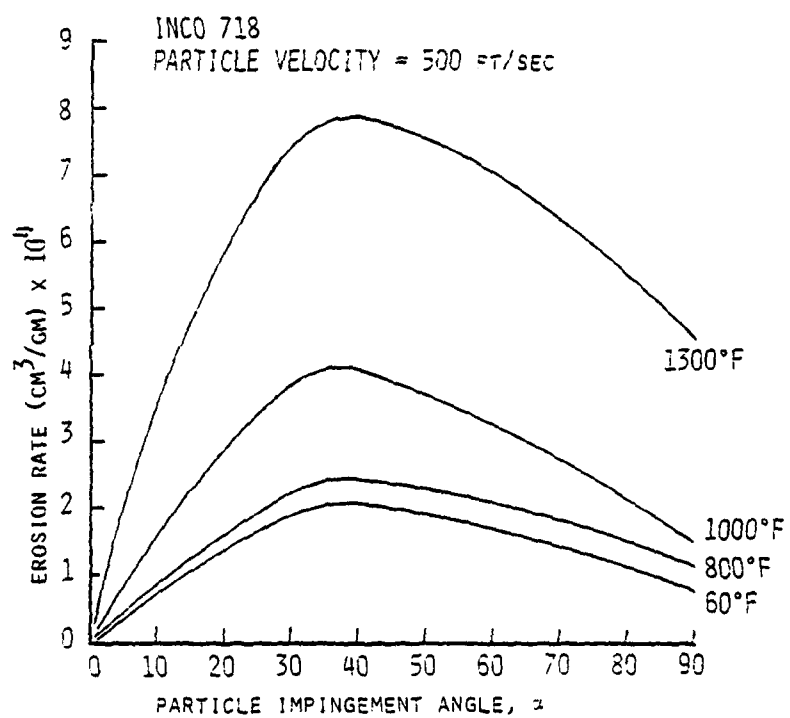   IMPINGEMENT ANGLE FOR DIFFERENT
           TEMPERATURES.

67

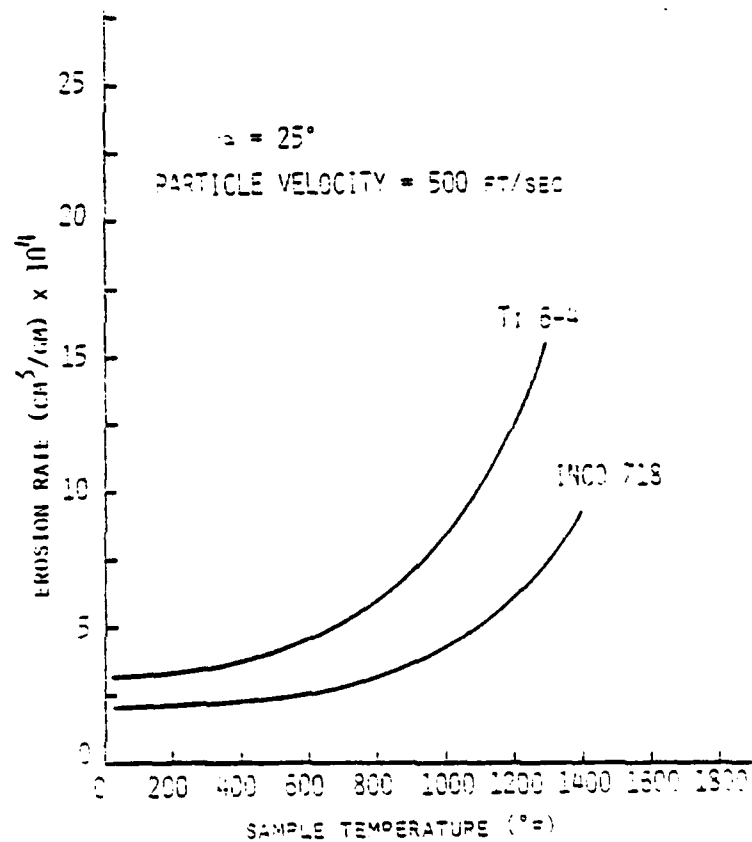FIG. 44. INCO 718 EROSION RATE VERSUS IMPINGEMENT ANGLE FOR
DIFFERENT TEMPERATURES.

68

FIG. 45.   Ti 6-4 AND INCO 718 EROSION RATE VERSUS
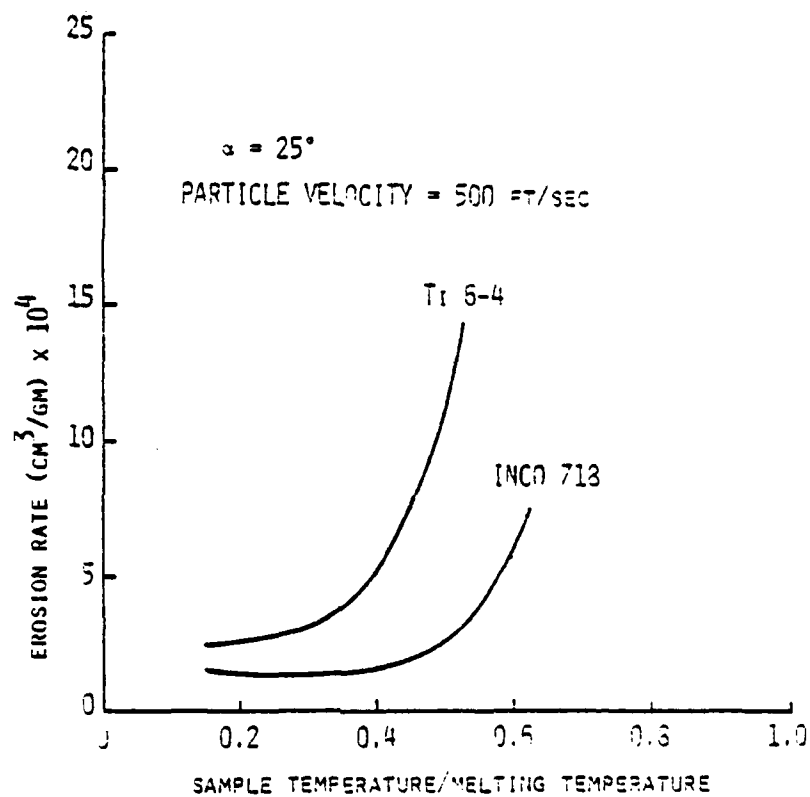SAMPLE TEMPERATURE, α = 25°.

FIG. 46. Ti 6-4 AND INCO 718 EROSION RATE VERSUS
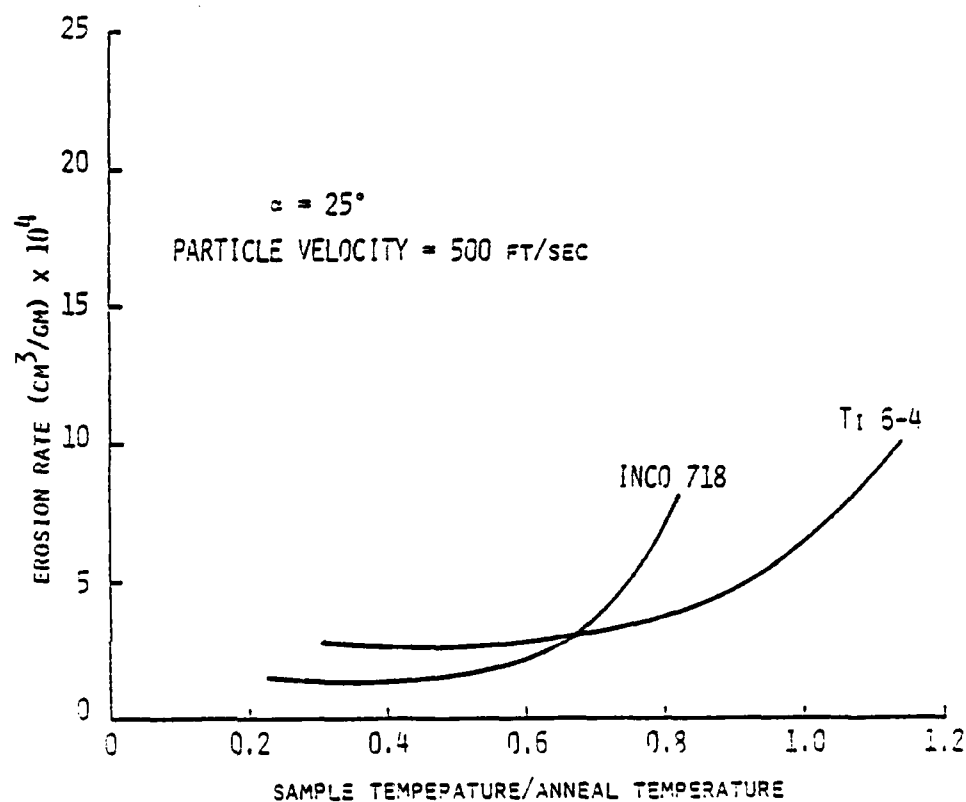SAMPLE TEMPERATURE/MELTING TEMPERATURE,
$\alpha = 25°$.

70

FIG. 47. Tı 6-4 AND INCO 718 EROSION RATE VERSUS SAMPLE TEMPERATURE/
ANNEAL TEMPERATURE, α = 25°.

SCIENTIFIC PERSONNEL SUPPORTED (PART-TIME)

BY THIS PROJECT DURING CONTRACT PERIOD

AND DEGREES EARNED

S. Abdallah - Graduate Research Assistant,
   Ph.D. Degree (1980).

R. Kotwal - Graduate Research Assistant,
   Ph.D. Degree (1980).

T. Wakeman - Graduate Research Assistant,
   Ph.D. Degree (expected 1982).

J. Ramachandran - Graduate Research Assistant,
   M.S. Degree (1979).

Y. Sheoran - Graduate Research Assistant,
   Ph.D. Degree (expected 1981).

W. Rudolph - Research Associate
   Postgraduate.

J. Lee - Graduate Research Assistant,
   M.S. Degree (1981).

R. Kandadai - Graduate Research Assistant,
   M.S. Degree (1980).

R. Hetico - Junior Research Assistant,
   B.S. Degree (1981).

LIST OF PUBLICATIONS AND PRESENTATIONS TO SCIENTIFIC MEETINGS

"Review of Material Erosion at High Temperature," presented
    to the ASTM Conference, Vail, Colorado, October 24-26,
    1977.

"Turbomachinery Affected by Environmental Solid Particles,"
    by T. Wakeman and W. Tabakoff, AIAA Paper No. 79-0041,
    presented to 17th Aerospace Sciences Meeting, New Orleans,
    La., January 15-17, 1979.

"Test Facility for Material Erosion at High Temperature," by
    W. Tabakoff and T. Wakeman," Erosion: Prevention and
    Useful Applications, ASTM STP 664, W.F. Adler, Ed.,
    American Society for Testing and Materials, 1979,
    pp. 123-135.

"Effect of Temperature on the Erosion of Metals," by N. Gat,
    W. Tabakoff and T. Wakeman, presented at 6th International
    Vacuum Metallurgy Conference on Special Melting and Metal-
    lurgical Coatings, San Diego, Cal., April 23-27, 1979.

"Particle Dynamics and Erosion in Turbomachinery," by W. Tabakoff,
    presented at 1979 International Gas Turbine Congress,
    Haifa, Israel, July 9-11, 1979. Paper No. 13, published
    in Congress Proceedings, 1980.

"Investigation of Metals Erosion in High Temperature Particulate
    Flows," by W. Tabakoff, published in Proceedings of
    Corrosion/Erosion of Coal Conversion Systems Materials
    Conference, published by National Association of Corrosion
    Energy, U.S. Department of Energy and Lawrence Berkeley
    Laboratory, July 1979.

"Effect of Temperature on the Erosion of Metals," by N. Gat,
    W. Tabakoff and T. Wakeman, Thin Solid Films, Vol. 64,
    1979.

"Temperature Effects on the Erosion of Metals Used in Turbo-
machinery," by W. Tabakoff, J. Ramachandran and A. Hamed,
published in Proc. of 5th International Conference on
Erosion by Solid and Liquid Impact, pp. 47-1 to 47-5,
Cambridge, England, September 3-6, 1979.

"Erosion Behavior in a Simulated Jet Engine Environment,"
by T. Wakeman and W. Tabakoff, Journal of Aircraft,
Vol. 16, No. 12, December 1979, pp. 828-833.

"Effects of Temperature on the Behavior of Metals Under
Erosion by Particulate Matter," by N. Gat and W. Tabakoff,
Journal of Testing and Evaluation, JTEVA, Vol. 8, No. 4,
July 1980, pp. 177-186.

PAPER SUBMITTED FOR FUTURE PRESENTATION

"Measured Particle Rebound Characteristics Useful for Erosion
Prediction," T. Wakeman and W. Tabakoff, to be presented
to the International Gas Turbine Conference, London,
England, April, 1982.

74

END

DATE

FILMED

8 1

DTIC

SUPPLEMENTARY

INFORMATION

AD-A103571

ERRATA

for Report No. 81-52, University of Cincinnati, entitled
"BASIC EROSION INVESTIGATION IN SMALL TURBOMACHINERY"

PAGE 23: In the first term on the right hand side of equations (13), (14) and (15), the following changes should be made:

For 2024 AL: $\varepsilon_V = 0.1076^{-4}$ should read $\varepsilon_V = 0.1076(10^{-4})$

For Ti 6-4: $\varepsilon_V = 0.149^{-4}$ should read $\varepsilon_V = 0.149(10^{-4})$

For INCO 718: $\varepsilon_V = 0.055^{-4}$ should read $\varepsilon_V = 0.055(10^{-4})$

PAGE 55, Fig. 27: The equations should read:

$$e_\beta = 1.0 - 0.000233 \, \beta_1^2 + 0.00000208 \, \beta_1^3$$

$$\sigma_{e_\beta} = 0.7905 - 0.02882 \, \beta_1 + 0.0004629 \, \beta_1^2 - 0.000002442 \, \beta_1^3$$

PAGE 56, Fig. 28: The equations should read:

$$e_v = 1.0 - 0.0179 \, \beta_1 + 0.000256 \, \beta_1^2 - 0.00000152 \, \beta_1^3$$

$$\sigma_{e_v} = 0.1785 - 0.00178 \, \beta_1 + 0.0000142 \, \beta_1^2$$

PAGE 57, Fig. 29: The equations should read:

$$e_N = 1.0 - 0.0211 \, \beta_1 + 0.0002278 \, \beta_1^2 - 0.000000876 \, \beta_1^3$$

$$\sigma_{e_N} = 0.362 - 0.00685 \, \beta_1 + 0.0000487 \, \beta_1^2$$

PAGE 58, Fig. 30:

$$e_T = 0.953 - 0.000446 \, \beta_1^2 + 0.00000648 \, \beta_1^3$$